PRELIMINARY INVESTIGATIONS INTO SELECTIVE LASER MELTING

A Thesis

presented to

the Faculty of California Polytechnic State University,

San Luis Obispo

In Partial Fulfillment

of the Requirements for the Degree

Master of Science in Industrial Engineering

by

David Takeo Otsu

June 2017

COMMITTEE MEMBERSHIP

TITLE: Preliminary Investigations into Selective Laser Melting

AUTHOR: David Takeo Otsu

DATE SUBMITTED: June 2017

COMMITTEE CHAIR: Xuan Wang, Ph.D.
Associate Professor of Industrial and Manufacturing Engineering

COMMITTEE MEMBER: Dan Walsh, Ph.D.
Professor Emeritus of Materials Engineering

COMMITTEE MEMBER: Katherine Chen, Ph.D.
Professor of Materials Engineering

ABSTRACT

Preliminary Investigations into Selective Laser Melting

David Takeo Otsu

Selective laser melting is a promising metallic additive manufacturing process with many potential applications in a variety of industries. Through a gracious donation made by Lawrence Livermore National Laboratory, California Polytechnic State University received and installed an SLM 125 HL selective laser melting machine in February 2017. As part of the initial setup effort, a preliminary machine verification study was conducted to evaluate the general print quality of the machine with default parameter settings. Coincidentally, the as-printed microstructure of SLM components was evaluated through nil strength fracture surface examination, an alternative to conventional polish-and-etch metallography. A diverse set of components were printed on the SLM 125 HL to determine the procedural best practices and inherent constraints. Additionally, the mode and mechanism of failure for a defective Lawrence Livermore National Laboratory component fabricated at their facility was investigated. From these studies, extensive documentation in the form of standard operating procedures, guidelines, templates, and summary reports was generated with the intent of facilitating future selective laser melting research at Cal Poly and strengthening the learning of students interfacing with the novel technology.

Keywords: selective laser melting, metallurgy, failure analysis, solidification

ACKNOWLEDGMENTS

First and foremost, I would like to thank my family for providing endless material, emotional and financial support throughout my entire existence. I owe everything to you. Thank you for being appreciative, understanding, and loving throughout the years.

I extend my utmost appreciation to Dr. Wang for giving me the opportunity to be your graduate student. The endless opportunities, encouragement, and support that you provided were unparalleled, and I could not have asked for a better advisor.

Thank you Dr. Chen and Dr. Walsh for the invaluable conversations that we shared. Your technical and personal advice guided me through this experience and enabled me to appreciate the many complexities of materials science and life as a whole.

Thank you Finley Marbury, Wyatt Hall, Angel Coria, Shaunessy Grant, Jake Whipple, Cole Nygren, Jordan Wright, Jesse Yap, Irene Yee, Kyle Devlugt, Thomas Pluschkell, Stephen Knaus, Steve Burke, and Matt Wraith for facilitating my technical efforts and providing endless challenges from which I could learn. Through our collaboration, I have become a better professional and engineer.

Thank you Lawrence Livermore National Laboratory for giving Cal Poly students the privilege to work with selective laser melting in a true learn-by-doing fashion. We are forever indebted to your contributions to our university.

Thank you Evan Dowey, Dominique Porcincula, Hajime Yamanaka, Katherine Adelman, and Chase Cooper for your companionship, company, and endless words of affirmation. In your own unique way, each of you has inspired me to be a better person. Friendship is rare, and I could not have asked for a better group of people to accompany me through my final year at Cal Poly.

Thank you everyone in the IME and MATE departments for allowing me to use your facilities and for putting up with my endless questions and mistakes. Your patience and understanding was more than I could have ever hoped for and I am honored to have the privilege of calling myself both an industrial and materials engineer.

For the countless individuals that I have not mentioned by name (MESS, MESSIDP, ESMAPE, and JSA members), know that you have made a positive impact on my life as well. Thank you for everything.

TABLE OF CONTENTS

LIST OF TABLES

Page

LIST OF FIGURES

Page

1 Introduction

Additive manufacturing (AM) is a broad category of processes in which a 3D object is fabricated through incremental additions of physical material. This may be directly contrasted with conventional subtractive manufacturing operations, such as turning, milling, and drilling.

Many specific AM processes exist across polymeric, metallic, ceramic, and composite material systems. Laser powder bed fusion (L-PBF), also known as selective laser melting (SLM), is a promising metallic AM process with growing applications in the aerospace, biomedical, and automotive fields. A thin, evenly spread layer of metallic powder is melted by a laser in a specified geometry to form a thin slice of continuous metal. The powder bed is then lowered and additional powder is spread evenly upon its surface. The laser melts the new powder layer, ideally joining the two thin slices to form a unified continuous piece of metal. This process of lowering the powder bed, spreading powder evenly across its surface, and melting the powder selectively with a laser is repeated until a fully solidified 3D object is formed.

Like other AM processes, SLM has a variety of unique advantages over conventional subtractive manufacturing processes. The time between computer-aided design to fabrication is significantly reduced, enabling fast-paced prototyping with a quick manufacturing turn-around time. Introducing complex geometries contributes negligibly to the overall processing time without requiring additional tooling, enabling designers to work with fewer monetary and temporal restrictions. Intricate channels that would otherwise be impossible to machine are easily fabricated, significantly broadening the design possibilities for metallic components.

Despite these advantages, SLM currently faces technical limitations that can only be overcome with considerable research. Certain geometries, such as overhanging surfaces greater than 45° from the build plate, cannot be reliably fabricated without considerable design modifications. Another example is thin-walled features (generally less than 0.3 mm), which have poor structural integrity and cannot be used for leak-proof applications. High aspect ratio components with sharp dimensional changes can exhibit crack-inducing residual stress without proper support structure and orientation planning.

The original intent of this thesis was to empirically optimize SLM parameter settings to successfully fabricate a component designed by Lawrence Livermore National Laboratory (LLNL). This goal depended on the rapid installation of the SLM 125 HL system at Cal Poly and the retrieval of accurate design information for the LLNL component. Unforeseen delays in the machine stand-up and the inaccessibility of design information led to a significant change in scope. The following are the finalized objectives of this thesis:

- Evaluate the general print quality of the SLM 125 HL with default parameter settings through a preliminary machine verification study,
- Study the as-printed microstructure of SLM components through nil strength fracture surface examination, an alternative to the conventional polish-and-etch metallography,
- Determine the mode and mechanism of failure for defective LLNL-identified components and recommend corrective actions for successful fabrication,
- Experiment with a diverse set of component designs to identify the SLM 125 HL best practices and overcome constraints inherent to the SLM process,

- Lay the foundation for future SLM research through extensive standard operating procedures and templates.

1.1 SLM 125 HL Hardware, Software, and Nomenclature

The SLM 125 HL is an SLM machine manufactured by SLM Solutions. It features a single 400 W IPG fiber laser with a 70 um – 100 um beam focus diameter. Components are produced in a 125 mm x 125 mm x 125 mm build volume with a 20 um – 75 um layer thickness. The atmosphere is rendered inert with a steady supply of high purity argon (SLM Solutions Group AG, 2017). Through a gracious donation made by LLNL, Cal Poly received and successfully installed a SLM 125 HL in February of 2017.

1.1.1 The Build Chamber

The main components of build chamber are as follows (Figure 1):

Build Plate – fabricated from 316L stainless steel and nominally 125 mm x 125 mm x 25 mm. Powder is spread on top of the build plate and melted with the laser to form a solid part. Build plates may be reused if the top surface is smooth and parallel to the bottom surface.

Elevator – Moves down by the pre-defined layer thickness as powder is spread and melted on the top surface of the build plate, which is fastened to its upward facing surface.

Recoater - dispenses powder evenly on the build plate with every pass. Held in place and actuated by the recoater carriage, which moves front-to-rear-to-front in the build chamber.

Powder chute - Directs powder from the feedstock container to recoater. Located at rear of chamber.

Air flow vents – directs laminar inert gas flow from the right to the left of the chamber. Blows away particles and soot thrown up by melting process.

Figure 1. The SLM 125 HL build chamber. A) The build plate and elevator. C) Recoater Carriage. D) Power chute. E) Air flow vents.

1.1.2 The Material System – 316L Stainless Steel

316L stainless steel is the only feedstock material used with the Cal Poly SLM 125 HL. In comparison to Al and Ti-based powders, 316L poses less of a safety hazard due to its low reactivity and negligible explosion risk (Murray, Cooper, & Nagy, 1964). The powder is supplied by SLM Solutions with accompanying physical and chemical certifications.

1.1.3 Laser Parameter Settings and Raster Patterns

The laser is capable of many different power, scan speeds, and beam focus diameter combinations (Materialise, 2015). Various energy density equations guide the selection of each of these parameters and are categorized into specific parameter sets. The type of parameter set utilized by the machine is dependent on the scan location within the slice polygon (Figure 2). In the simplest form, each slice polygon has two main sections: the outer border, which is melted with contour scans, and the inner body, which is melted with fill scans.

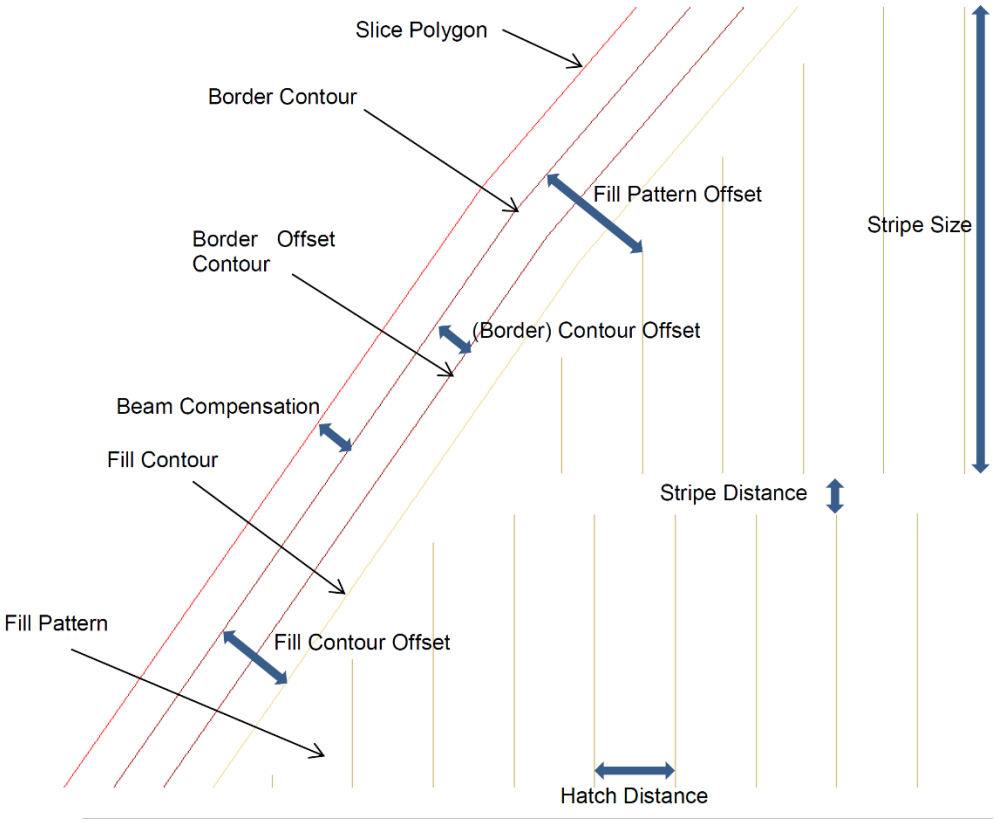

Figure 2. Various scan categories as defined by the SLM Build Processor module.

The first and simplest of the two main fill scan strategies is stripe. The laser scans in straight, parallel lines from one polygon slice edge to the other until the entire body is filled. The second fill can strategy is chess, in which the inner body is divided into

equally sized and evenly distributed squares. Every other square is melted using straight, parallel lines in one overall direction. The remaining squares are then melted using straight, parallel lines in a direction perpendicular to the first. This results in a melted surface that resembles a chessboard.

In general, the stripe parameter set produces components up to 30% faster than chess and can result in a more continuous microstructure. Conversely, chess heats the component more evenly, lowering the component's residual stress, thereby mitigating delamination or peel-off. Depending on the geometry of the component being printed, both scan strategies have their uses and limitations.

1.1.4 Orientation Axes as References

The orientation axes used in this report to describe the build environment as viewed from the front door are as follows (Figure 3):

X-axis – runs from left side to right side of build chamber

Y-axis – runs from front side to rear side of build chamber

Z-axis – runs from build platform to top of build environment

As a result, each powder layer runs parallel to the XY-plane and are laid on top of each other in the Z-direction.

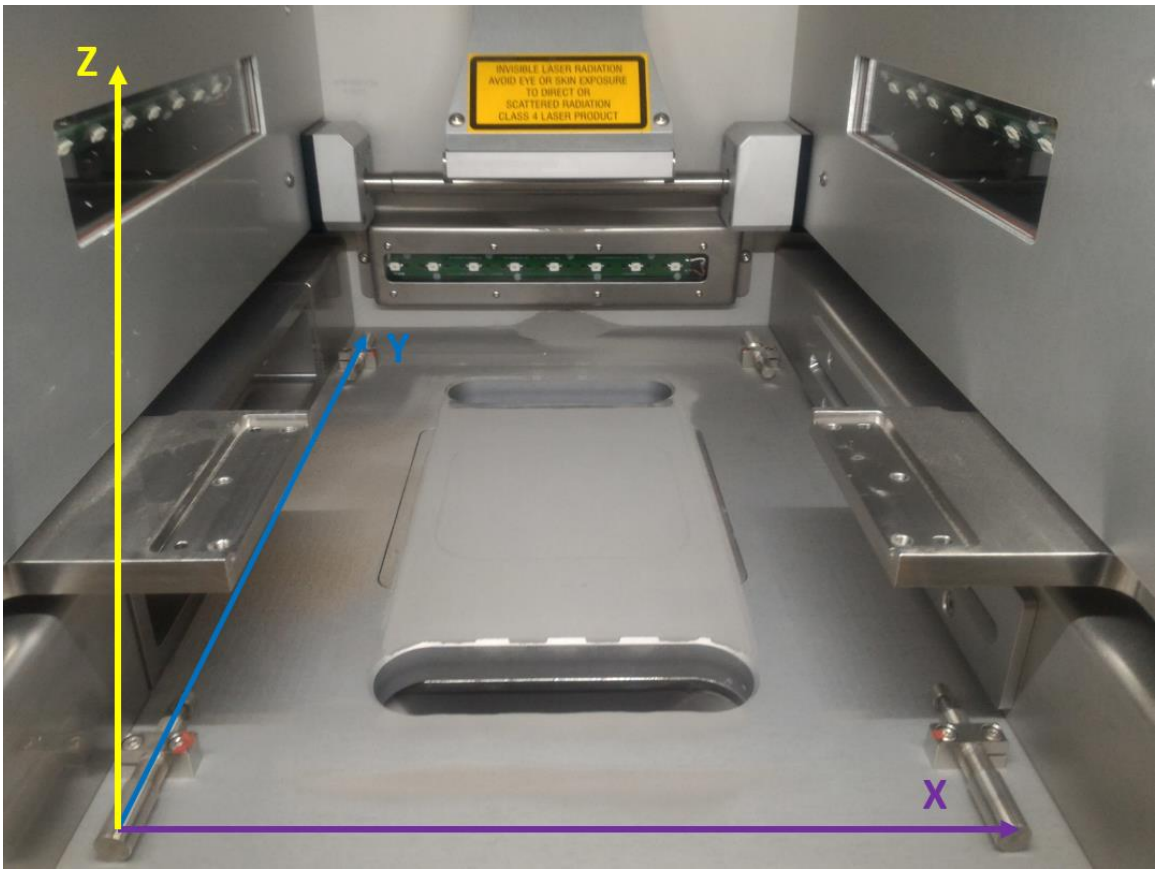

Figure 3. Orientation axes relative to the build chamber.

1.1.5 Component Surface Types and the 45° Angle Rule

Three surfaces are defined by their angle relative to the build plate in order to differentiate the challenges unique to each surface's formation mechanism and subsequently tailor the associated laser parameters. There are as follows:

Vertical surfaces - surfaces that are exactly 90° relative to the build plate

Upward facing surfaces – surfaces that are greater than 90° relative to the build plate

Downward facing surfaces – surfaces that are less than 90° relative to the build plate (also known as overhanging surfaces)

The SLM 125 HL reserves special laser parameters known as the up-skin and down-skin for the upward and downward facing surfaces, respectively. As a general rule of thumb, downward facing surfaces that are less than 45° relative to the build plate must be printed with support structures that provide a connection between the component surface and the build plate (Figure 4). Without support structures, the laser may over-penetrate when fabricating the critical overhanging surfaces, resulting in melt percolation and a drastically reduced surface finish quality.

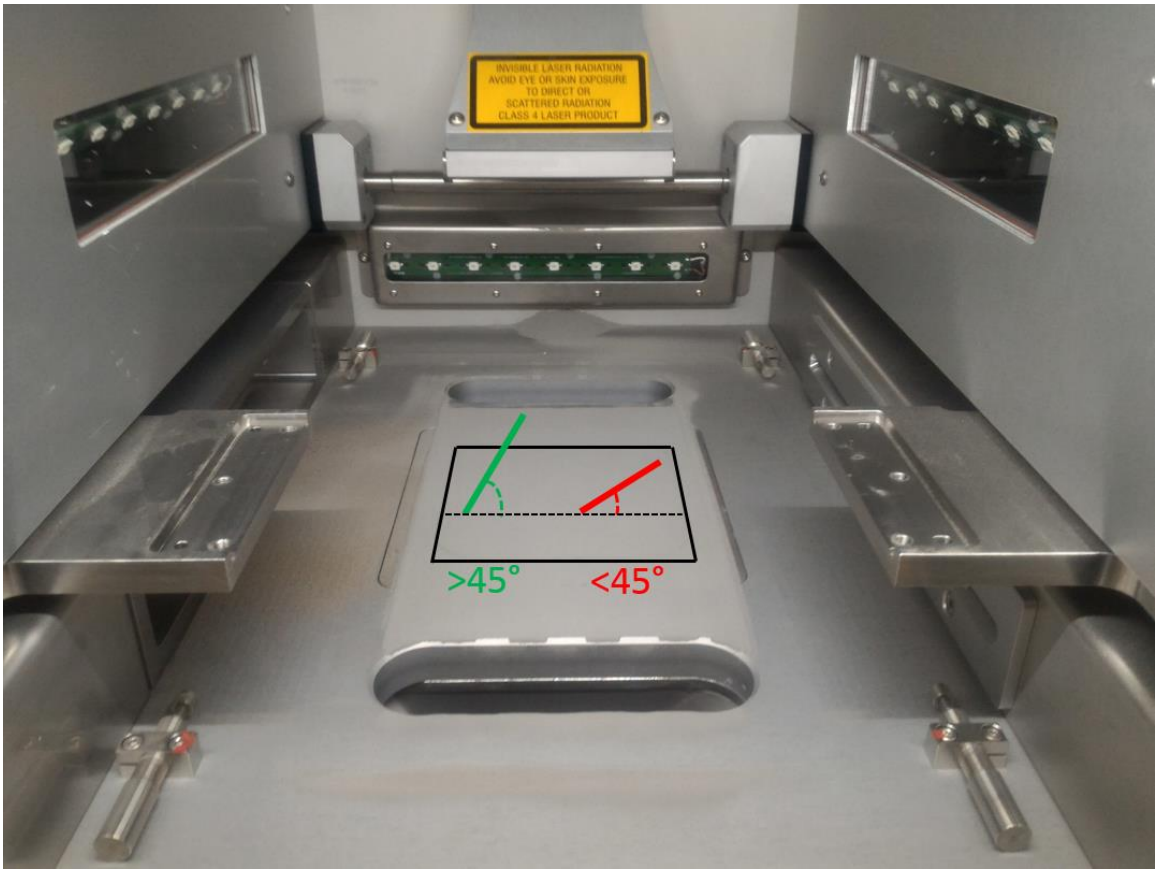

Figure 4. Schematic depicting the 45° angle rule.

1.1.6 Support Structure Types

Three support structures have been evaluated at the time of writing:

1.1.6.1 Line

The line-type support structure generates a single vertical wall with triangular connection sites on the downward facing surface and build plate. Accompanied with fins to stabilize the wall in out-of-plane bending. As was discovered in Section 5.4, the line support structure is only suitable for downward facing edges, as actual surfaces require more interfacing area to prevent significant melt percolation.

1.1.6.2 Block

The block-type support structure generates vertical walls in a grid pattern. The supports interface with the downward facing surface at the grid intersections, resulting in a cross-column connection point. Although the block-type is a well-rounded general purpose support structure, it consumes the largest volume of material, takes the longest to print, and is the most difficult to remove in post-processing.

1.1.6.3 Contour

The contour-type support structure generates a vertical wall that follow the border of the overhanging surface. Moving towards the center of the overhanging surface, the contour-type continues to generate, smaller vertical walls along each consecutive border until the entire surface is filled with support structures. While more efficient with material usage in comparison to the block-type, auto-generating contours often results in large gaps between each vertical border wall and must be manually supplemented by the SLM operator.

1.2 The Idea to Print Process

All designs start with an idea, and some ideas are better suited for the SLM process than others. For example, concepts necessitating complex internal cavities, unusual curvatures, or features unique to each individual component would likely manufacture better through the SLM process versus conventional subtractive manufacturing. The idea begins its digital life in computer aided design (CAD). The designer must be aware of the limitations of the machine and should envision how the part will be oriented, positioned, and supported within the SLM build volume. Additionally, the designer must consider how excess powder will be removed from internal cavities and the ease at which post-processing techniques can be performed.

The completed and valid-for-SLM CAD model is exported as an .STL into the Magics Software Suite. Magics models the build envelope and allows one to place and orient parts as they will be printed during the SLM process. Its support structure generation module may be used to address critical downward facing surfaces by through the addition of interfacing supports (see Section 1.1.6 for more information). Once the laser scan strategy is set in the SLM Build Processor module, the entire build environment is digitally sliced, exported to a .SLM file, and exported to the SLM 125 HL.

Most laser-independent parameters are set in the Machine Control software. The major parameters of interest are as follows:

- Build plate temperature (120°C default)
- Powder volume to dispense per layer (4 chambers default)
- Minimum recoater cycle time (15 seconds default)

- Chamber pressure (70 mbarr default)
- Argon flow rate (varies based on filter status)

Once the parameters are set and the machine is completely set up for manufacturing operations, the build is initialized. A detailed step-by-step guide for the SLM process is provided in standard operating procedures on the Dozuki platform as is discussed in Section 6.

2 Preliminary Machine Verification Study

Based on the parent company's product history, most SLM technologies currently on the market are considered 2nd generation machines. Because of this, general functionality and technological competitive advantage is valued over extreme consistency between products of the same model. The consequences of this become clear during normal operation. For example, LLNL has observed functionally identical assemblies consisting of dissimilar components in their serially-sequential M2 ConceptLaser machines.

Based on such observations, a strong argument is made for treating each machine as its own unique system. SLM Solutions provides basic parameter suites for each of its supported material families along with expected baseline physical and mechanical properties. It is unlikely that the basic parameter suite is the most optimal for any given machine, including Cal Poly's. For this reason, a machine verification study was conducted to evaluate the quality of the parts produced using the default parameter set and to determine if further parameter optimization for general usage is necessary. Due to time constraints, only a small preliminary study has been completed at the time of writing. The recommended path forward for a complete machine evaluation is provided in Section 2.4.

2.1 Experimental Design and Procedure

Three physical responses were identified as suitable representations of general print quality: surface morphology, microstructure, and bulk density. Additionally, the tensile mechanical properties and the accompanying fracture surfaces were also analyzed. Unless otherwise stated, all parts were raised 5.0 mm above the build plate by the default "Block" support structure type and excised with a coolant-sprayed horizontal band saw.

2.1.1 Physical Analysis Cube and Print Details

A basic 20 mm x 20 mm x 20 mm Physical Analysis Cube (PAC) was modelled in Magics to evaluate the aforementioned physical responses (Figure 5). 2 PACs, denoted PAC-A-1 and PAC-A-2, were printed as part of Build A with the default stripe parameter set and supported 3.0 mm above the build plate with a modified block-type support structure. The build completed without any complications arising from the component's design.

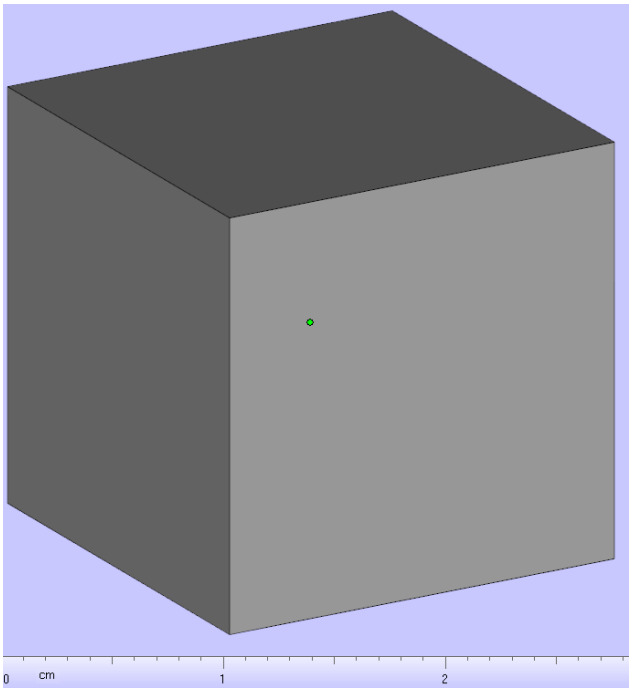

Figure 5. CAD model of the Physical Analysis Cube.

The PACs from Build A showed considerable degradation around the corners and edges of their downward facing surfaces. Moderate surface burn-in accompanied the degradation at the interface of the support structure and the cube. These observations were considered outside the acceptable operational envelope by the SLM technician present. Despite this, the decision was made to continue with the planned physical analysis (Figure 6).

An additional PAC was salvaged from an unfinished chess parameter set Z-orientation tensile block on Build B. This block, denoted PAC-B-1, shared the same build environment as the Build B Mechanical Analysis Rectangular Prisms (2.1.2).

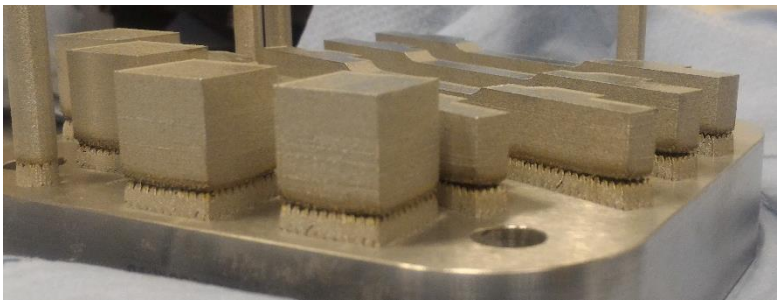

Figure 6. Post-fabrication image of Build A. Significant burn-in and delamination apparent at the interface between the components and support structures.

2.1.2 Mechanical Analysis Rectangular Prism and Print Details

The first tensile bar design was based on the ASTM E8 sub-sized rectangular tensile bar (Figure 7). Since the surface roughness of as-printed SLM material falls outside of the acceptable ASTM E8 range, the thickness of all surfaces was increased by 0.05” to enable post-print machining of the bars to final dimensional specifications. Additionally, two 0.7” x 2.5” tabs were added to the grip sections of the bar to facilitate fixturing. 4 modified tensile bars were printed as part of Build D with the default stripe parameter set and supported 3.0 mm above the build plate with a modified “Block” support structure type. The build completed without any complications arising from the component’s design.

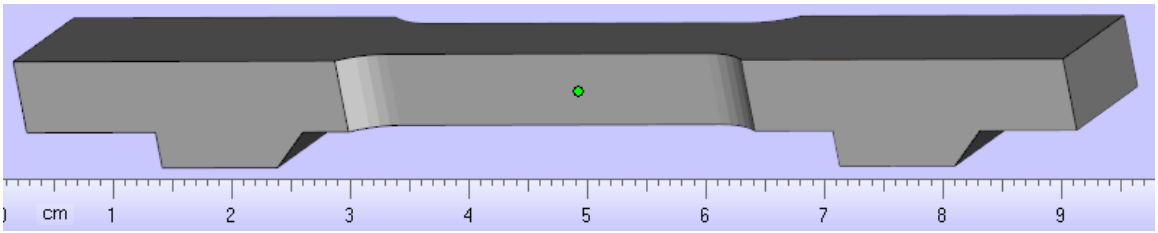

Figure 7. CAD model of the modified ASTM E8 subsize tensile bars. Fixturing tabs protrude from the side of the grip sections.

The length-wise continuous laser raster inherent to the stripe parameter set resulted in high contractual residual stress on cooling. Subsequently, the high-aspect ratio tensile bars peeled off from the support structures, resulting in significant bowing (Figure 8). In this condition, the bars were too warped to machine to specification, necessitating a different approach.

Figure 8. Warped modified tensile bars with burn-in and degradation along the downward facing surface.

To reduce the contractual residual stress, another 4 bars were fabricated as part of Build E with the default chess parameter set. These printed successfully with minimal

warpage. However, machining difficulties revealed that the tabs were too small for proper fixturing, necessitating an entirely new design.

To add more material for machining operations, the second tensile bar iteration was simplified to a 104 mm x 11.5 mm x 11.5 mm Mechanical Analysis Rectangular Prism (MERP) from which the ASTM E8 subsize tensile bars are excised (Figure 9). 4 MERPs were printed with the default chess parameter set as part of Build B. A second set of 4 MERPs were successfully printed with the default chess parameter set as part of Build C.

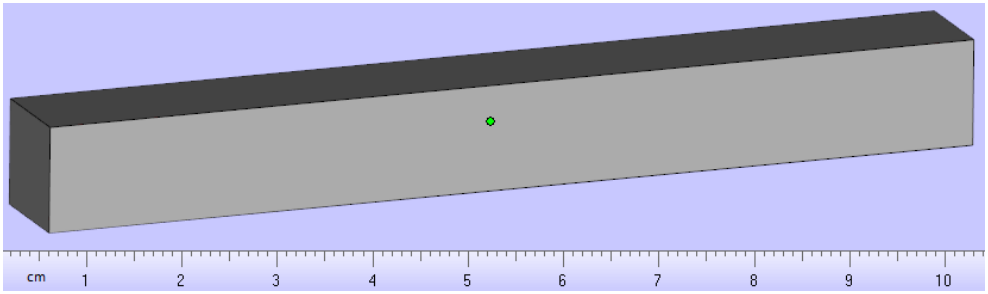

Figure 9. CAD model of the Mechanical Analysis Rectangular Prism.

2.1.3 PAC Post-Processing and Analysis

The surface morphologies of the PACs were analyzed with a FEI Quanta 200 Scanning Electron Microscope (SEM). After SEM analysis was complete, the surfaces were machined using a TiN-coated carbide end mill to achieve a smooth and uniform surface finish. A pair of calipers and a mass balance were used to measure the PAC volume and mass, respectively. These measurements were then used to calculate the effectively density of the PACs. The PACs were then sectioned along the YZ plane, mounted in bakelite, ground, polished, and electrolytically etched with an oxalic reagent.

2.1.4 MERP Post-Processing and Analysis

The MERPs were placed in an air-tight 303 stainless steel bag and heat treated at 1040°C in a standard atmosphere furnace for 2 hours and left to air cool overnight. The MERPs were machined to the ASTM E8 subsize rectangular bar specification using a TiN-coated carbide end mill. The bars were mechanically tested with an Instron Universal Testing Machine. A single near-net tensile bar from Build E (E-1) was also mechanically tested (Table 1). The fracture surfaces of the bars were examined with a FEI Quanta 200 Scanning Electron Microscope.

Table 1. Catalog of Specimens Printed

Specimen	Dimensions	Build	Parameter Set	Quantity Tested
Physical Analysis Cube	20 mm x 20 mm x 20 mm	Build A	Stripe	2
		Build B	Chess	1
Mechanical Analysis Rectangular Prism	104 mm x 11.5 mm x 11.5 mm	Build B	Chess	4
		Build C	Chess	4
		Build E	Chess	1

2.2 Results and Discussion

This section overviews the results of this study and discusses any and all implications.

2.2.1 Surface Finish

SEM analysis of the PACs show adhered particles covering 15% – 20% of the part's surface. The majority of particles (>90%) are spherical, with a small fraction (<5%) consisting of two or more particles partially melted together to form mild agglomerates. Mild ridges on the solidified surface are observable on the vertical wall surfaces, likely corresponding to each layer's contour laser scan. The surfaces are absent of cracks or delamination (Figure 10).

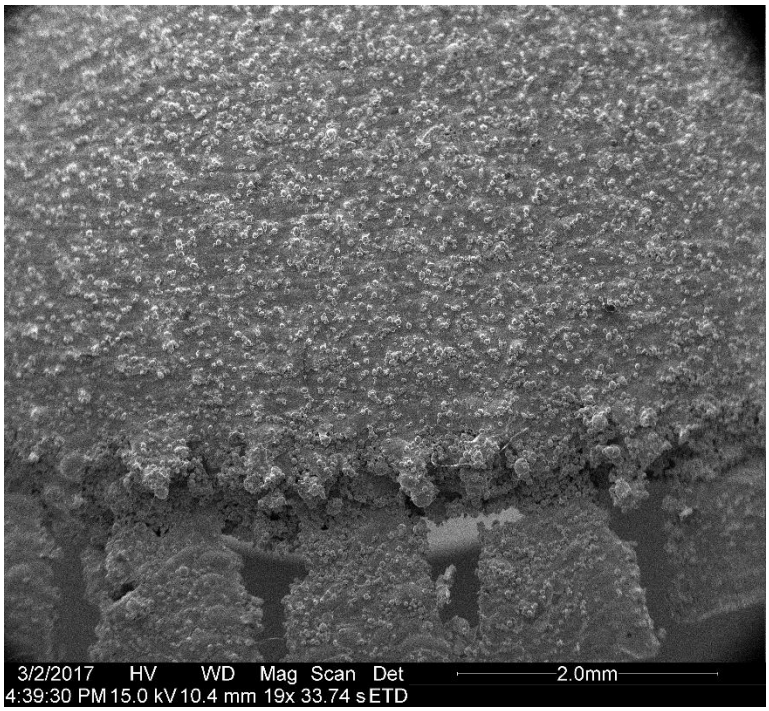

Figure 10. SEM image of the vertical wall of PAC-A-1. Remnants of the support structure protrude from the cube at the bottom of the image.

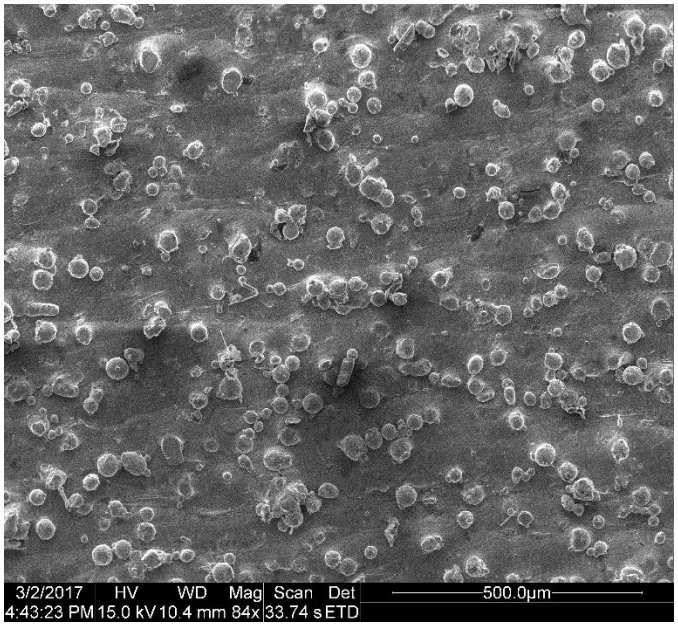

Figure 11. SEM Image of the vertical wall of PAC-A-1. Particles cover 15-20% of the cube's surface. Surface is free of delamination or discontinuities, at most exhibiting mild bumps between layers.

Figure 12. SEM image of particles adhered to the surface of the vertical wall of PAC-A-1.

With fewer adhered particles and less-pronounced discontinuities between layers along the vertical walls, the surface finish produced by the SLM 125 HL is superior to those produced by the ConceptLaser MLab or EOS M270 machines as seen in literature (Otsu, Muetterties, & Lovejoy, 2016; Strano, Hao, Everson, & Evans, 2013). This, along with absence of cracks or delamination, is enough evidence to conclude the surface finish produced by the machine is at an acceptable standard of quality. More specifically, the contour laser parameter sets are satisfactory for vertical walls. This claim may be generalized to future parts with different inner volume laser parameters if it may be safely assumed that the two scan regions do not significantly interact.

2.2.2 Density

First and foremost, the succeeding fracture surface analysis in Section 2.2.5 revealed significant porosity concentrated along the inner edges of the fabricated components. Since all PACs were machined before volume and mass measurements were taken, a significant amount outer layer thickness material was removed. Therefore, these

results are only relevant to the general bulk porosity of the specimens corresponding to the fill laser scan area. Recommendations for measuring the inner edge porosity are made in Section 2.4.

Using 8000 kg/m^3 as the baseline density for 316L stainless steel, porosity measurements from PAC-A-1 and PAC-A-2 were 0.89 vol% and 0.90 vol%, respectively. Conversely, B-1 exhibited a much higher porosity measurement of 4.11 vol% (Table 2).

Table 2. PAC apparent density measurements.

Specimen	Parameter Set	Volume (cm^3)	Mass (g)	Apparent Density (g/cm^3)	Vol% Porosity
PAC-A-1	Stripe	3.123	24.764	7.929	0.89
PAC-A-2	Stripe	1.818	14.394	7.913	0.90
PAC-B-1	Chess	1.819	13.951	7.665	4.11

SLM solutions claims up to 99.9% density under optimal fabrication conditions for 316L stainless steel components made with the SLM 125 HL (SLM Solutions Group, 2014). At an average of 0.895 vol% porosity, the Build A specimens are near the acceptable bulk density levels. On the other hand, the porosity in the Build B specimen is higher by a significant margin. If it is assumed that the porosity seen in the fracture surface analysis of the accompanying Build B tensile bars is the same as the porosity in the B-1 PAC specimen, it is reasonable to say that the 4.11 vol% is a valid measurement.

The difference in porosity between Build A and Build B may be correlated with the fabrication parameter set, general variance between builds, or both. With so few data points with confounding factor interactions, it is difficult to identify the reason for the difference in porosity. This, combined with the results of Section 2.2.5.2, is compelling

enough to recommend a parameter optimization study with the goal of reducing general component porosity as is outlined in Section 2.4.

2.2.3 Microstructure

Due to poor etch quality, it is difficult to observe any structures above 50 um in scale. For this reason, the weld solidification structures that are expected to be 100 um – 1000 um in characteristic length are left unobserved in this study. Instead, the focus of the metallographic analysis is on the grain sub-structure at the 1 um – 10 um characteristic length scale.

An intergranular network of cells 0.5 um – 2 um in characteristic length are found within each individual grain (Figure 13). Based on compositional EDS analysis in literature, the cells are high in carbon and low in chromium (Cr) and molybdenum (Mo) while the cell borders are rich in Cr and Mo and low in carbon. As 316L is an austenitic stainless steel, it is believed that the cells are austenite (Saeidi, 2016). Conversely, since Cr and Mo are ferrite-stabilizing elements, it is believed that the cell borders are delta-ferrite.

Neighboring the cellular regions are high aspect-ratio, parallel sub-structures resembling layers or elongated columns. Based on literature, these structures are believed to be the transverse view of the cellular networks.

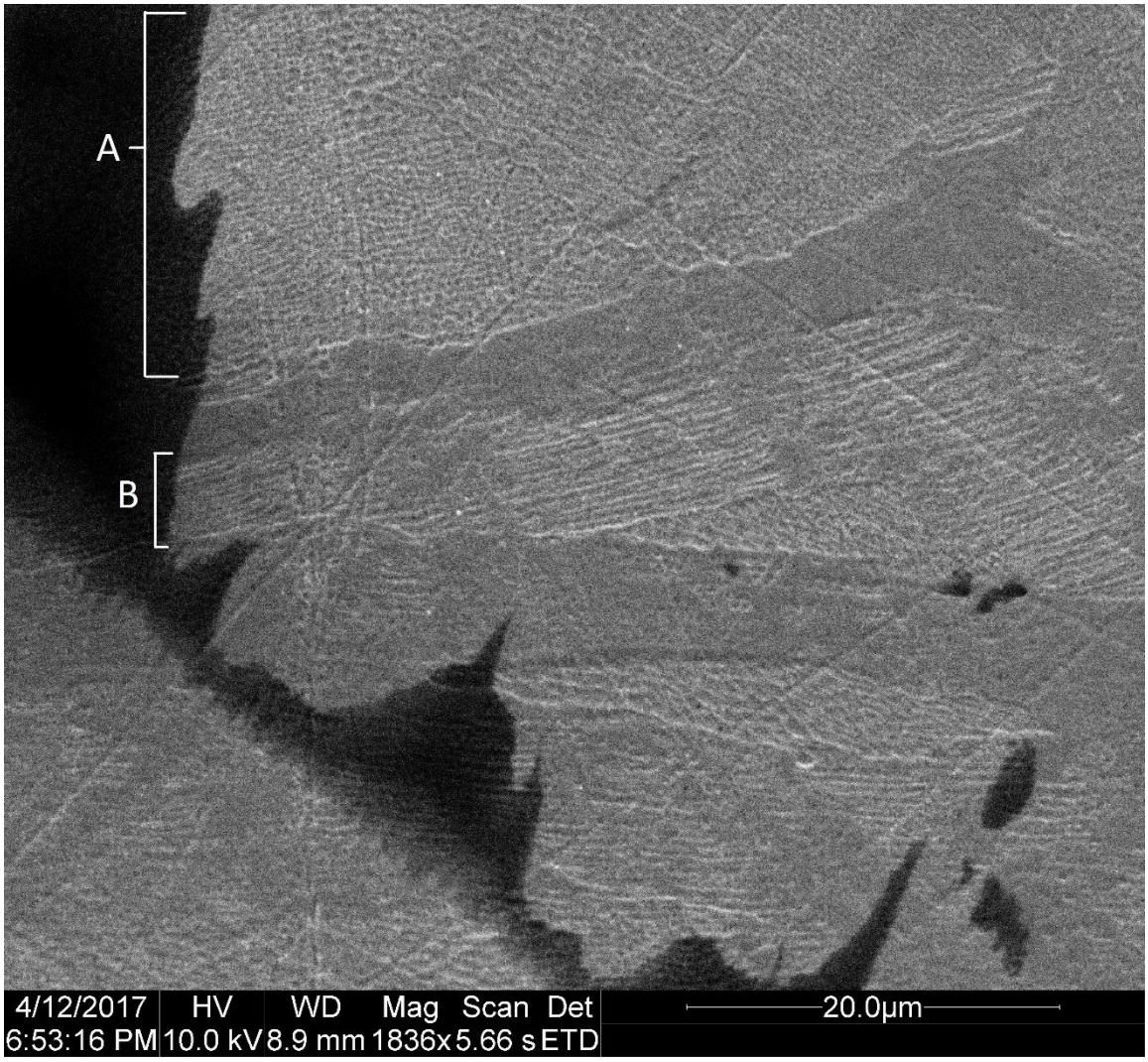

Figure 13. SEM image of oxalic etched metallographic PAC-A-1 specimen at the interface of a pore. A) Cellular network sub-structure. B) High aspect-ratio, parallel sub-structures.

The sub-structures reported in literature reflect those seen in the Cal Poly PAC specimens (Montero Sistiaga, Nardone, Hautfenne, & Van Humbeeck, 2016; Zhong, Liu, Wikman, Cui, & Shen, 2016). This suggests that the solidification rates of each individual weld and the general chemistry of the 316L powder feedstock is nominal. It is recommended to verify the 100 um – 1000 um scale weld microstructure in a follow-up study (see Section 2.4).

2.2.4 Tensile Properties

All Build B specimens and specimens C-1 and C-4 from Build C were mechanically tested without any complications (Figure 14). The strain gauge on specimens C-2 and C-3 slipped during testing, invalidating their mechanical property results. The valid data exhibited low variation, with an average Young's modulus of 207.2 GPa, 0.2% offset yield strength of 375.87 MPa, Ultimate tensile strength of 636.8 MPa, and % elongation of 32.45% (Table 4).

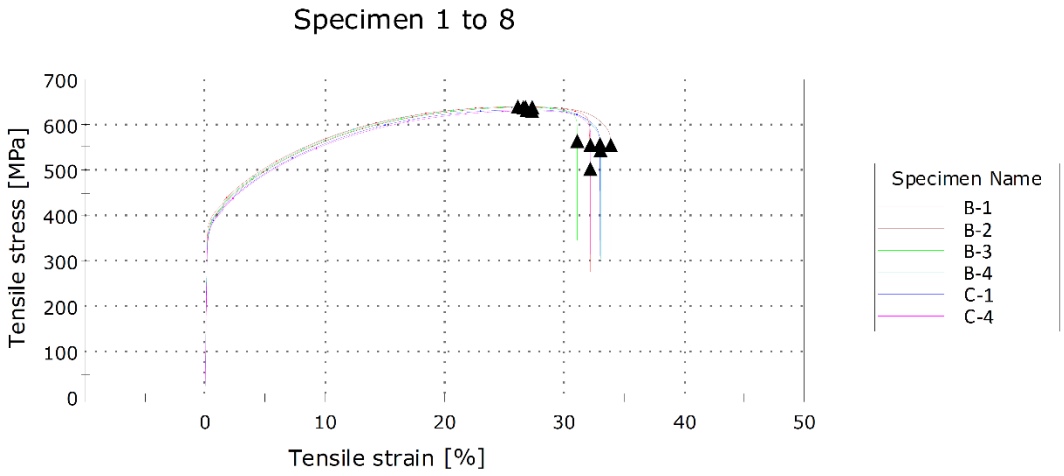

Figure 14. Stress-strain curve of valid tensile specimens.

Table 3. MERP Mechanical Test Results

Specimen	Young's Modulus (GPa)	0.2% Offset Yield Strength (MPa)	Ultimate Tensile Strength (MPa)	Elongation (%)
B-1	202.38	388.4	640.1	32.07
B-2	207.37	374.8	639.1	33.78
B-3	211.39	375.6	638.4	30.98
B-4	210.21	378.7	639.4	32.93
C-1	215.45	369.5	633.2	32.88
C-2	Invalid			
C-3	Invalid			
C-4	196.41	368.2	631.0	32.08
Average	207.2	375.87	636.87	32.45
Std Deviation	6.85	7.3	3.39	0.96

The yield and ultimate strength of the heat treated bars are comparable to annealed SLM material in literature (Montero Sistiaga, Nardone, Hautfenne, & Van Humbeeck, 2016). Both strengths are higher than wrought 316L stainless steel in the annealed condition (Washko & Aggen, 1990). Post-heat treatment microstructural analysis with side-by-side wrought comparisons would likely reveal the source of this difference, such as average grain size and the corresponding grain boundary strengthening.

Conversely, the % elongation of the Cal Poly specimens are significantly lower than both the annealed SLM 316L results seen in literature and wrought 316L in the annealed condition specifications (Washko & Aggen, 1990). The difference is too great to explain away with strength-ductility trade-offs resulting from insufficient annealing. Observations from the fracture surface analysis (Section 2.2.5) reveal significant porosity, likely resulting in the % elongation knock-down.

2.2.5 Fracture Surfaces

2.2.5.1 As-Printed, No Heat Treatment

The as-printed tensile bar from Build E exhibited a ductile fracture surface with significant spherical porosity along the interior of the vertical walls (Figure 15). This phenomenon has been seen in literature and should not necessarily be considered highly unusual or out of specification (Yusuf, Chen, Boardman, Yang, & Gao, 2017). Occasional unmelted particles in the bulk of the component and an associated circular void are seen. There is no evidence of significant delamination or patterned internal porosity within the inner section of the component corresponding to the fill laser patterning.

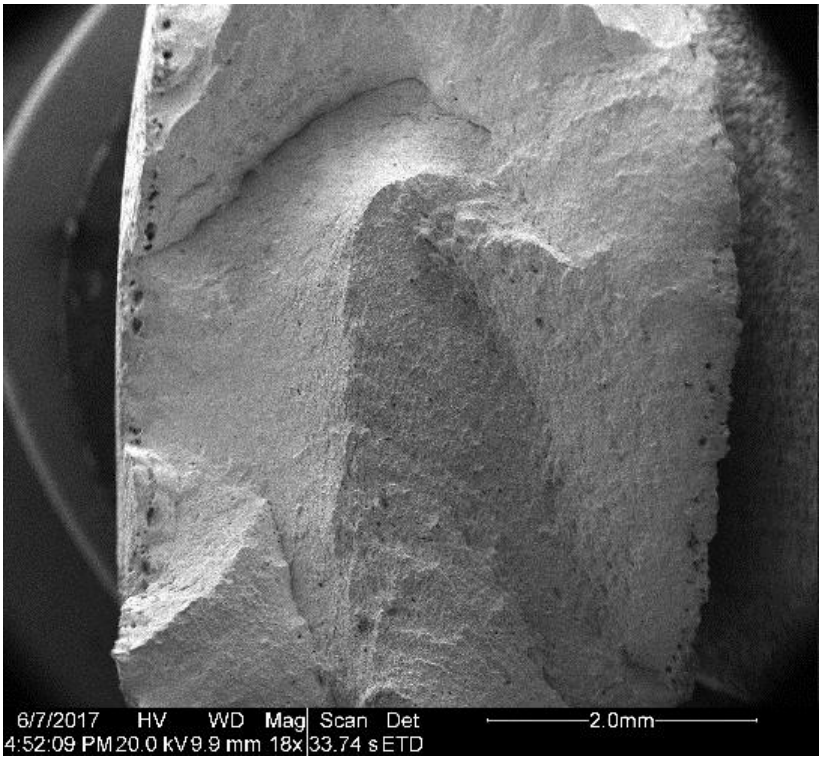

Figure 15. SEM image of fracture surface of the as-fabricated tensile bar (E-1) printed with the chess parameter set. Spherical porosity lines the interior of the vertical walls.

The spherical voids along the vertical walls are located interior to the contour scan path and exterior to the fill scan path. The parameters and scans associated with this region are the border offset contour, the fill contour, and the fill contour offset. It is unlikely that the energy density in this region is too low or that the offset is too large, as there would be unmelted particles accompanying the spherical pores. If the energy density is too high, the recoil forces caused by metal ablation may be destabilizing the weld pool, causing air to be trapped during solidification. Alternatively, if the offset spacing is too low, the fill contour and fill scans that follow the outer contour scans would remelt the existing weld tracks without sufficient feedstock powder from the surrounding areas, resulting in incomplete weld tracks. This may be aggravated if the earlier contour scan denudates powder in the surrounding region (Matthews, et al., 2016).

Additionally, there is always the possibility that the pores formed during mechanical testing. Since the pores are offset from the edge at a constant length, it is reasonable to believe that any strain-induced porosity formed is a consequence of microstructural initiation sites formed during the fabrication process.

It is recommended to investigate the inner edge porosity phenomenon in follow up studies, as the presence of pores will likely have a detrimental effect on mechanical properties. See Section 2.4 for the suggested path-forward towards minimizing the problem.

2.2.5.2 Block, Heat Treatment

Fracture surface analysis of Build B specimens revealed significant high aspect-ratio porosity (Figure 16). The major axis of the pores run parallel to the XY plane, corresponding to the layers laid down during the process. The walls of the pores are

smooth, solidified structures, with no evidence of yield or fracture as a result of mechanical testing (Figure 17). The majority of the pores contain unmelted particles adhered to the outer edges. None of the pores show patterning or aligning with respect to the Z-axis.

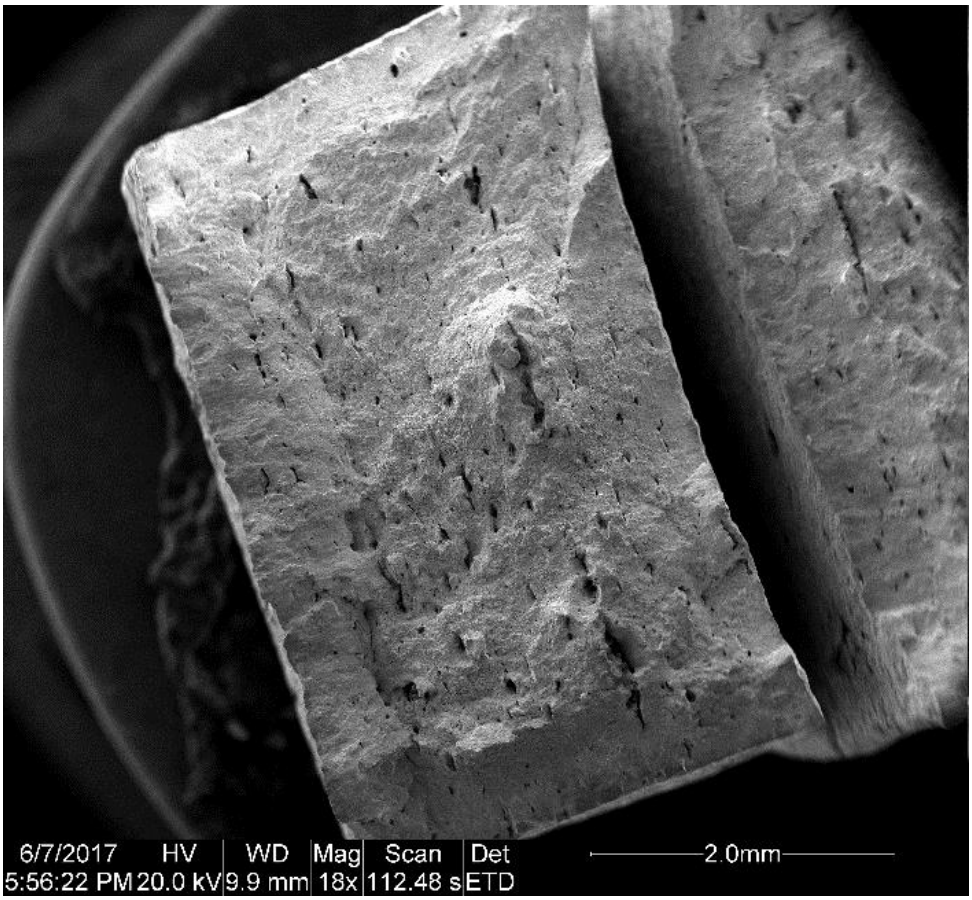

Figure 16. SEM image of the fracture surface of specimen B-2 printed with the chess parameter set. High-aspect ratio pores indicative of delamination span the XY layer plane.

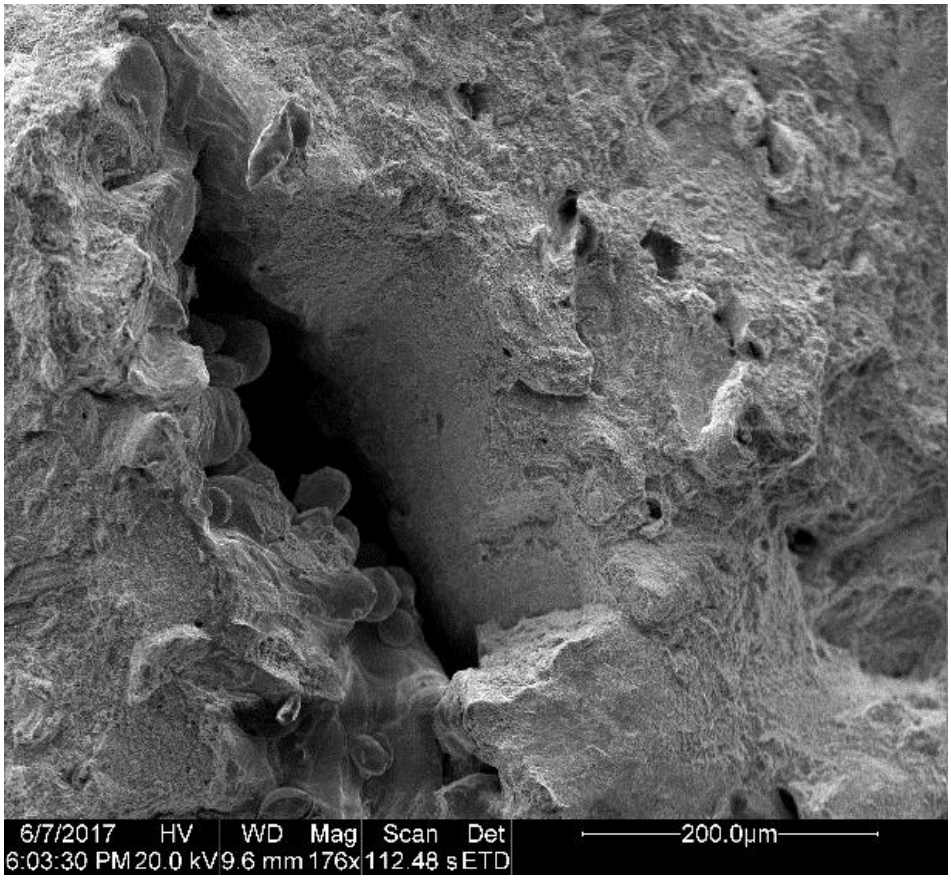

Figure 17. SEM image the of interior of a high-aspect ratio pore from specimen B-2 printed with the chess parameter set. Pores adhered to a solidified surface suggest the pore was not mechanically induced or the result of hot cracking .

The presence of particles adhered to the solidified walls of the pores indicates that the pores formed due to insufficient melting and are therefore not the sole by-product of mechanical testing. Moreover, the shape of the pores and the alignment of the major axis to the XY plane of printing suggests the pores are the result of delamination caused by insufficient coalescence between layers. Although pore formation may be intensified by hot cracking and the observations made during the nil strength fracture surface analysis in Section 4.2 shows a propensity towards initial continuous liquation between layers, it is unlikely that this is the primary mode of failure, as the presence of unmelted particles within the pores indicates that the regions never fully melted and coalesced at any point.

Partial coalescence between layers may be the result of inadequate weld penetration caused by insufficient volumetric energy density. Metallographic cross-sections of individual weld tracks may reveal the approximate depth of penetration. This, in combination with a volumetric energy density study at the bulk component level, should help develop a proper parameter setting envelope for near-dense parts. Recommendations for this are made in Section 2.4.

Alternatively, the delamination may be caused by sub-regions of the inner slice volume being omitted from the laser scan path due to errors in the pattern generated by the SLM software. This may be due to specific regions of the fill pattern (e.g. along the edges of the chess squares) being at greater risk of insufficient melting. Testing for detrimental phenomena related to the fill scan is difficult, as the pattern rotates and shifts between each layer to reduce overall anisotropy. For this reason, the fill pattern would have to be fixed to repeat at a known cycle period. Doing so would allow CT scans or careful cross-sectioning to check the spatial porosity distribution and correlate it to specific regions within the scan pattern. As this is either time-intensive or outside the capabilities of Cal Poly facilities, it is not recommended to conduct a study to investigate scan-pattern related theories.

2.3 Conclusions

A preliminary study was conducted to evaluate the quality of components printed by the SLM 125 HL under default laser parameter settings. The surface morphology and its associated contour scan path are of acceptable quality. Microstructural analysis shows 0.5 um – 2 um scale sub-structures that match literature results, indicating nominal individual weld solidification rates and acceptable powder feedstock compositions. Due

to inadequate etchant quality, observations and conclusions about the larger 70 um – 1000 um weld solidification structures cannot yet be drawn. The 0.2% offset yield strength and ultimate tensile strength are satisfactory when compared to SLM in literature and wrought 316L material. However, % elongation is below the expected limit. Fracture surfaces show significant spherical inner edge porosity and inner bulk delamination. This corresponds with the less than optimal effective density measurements taken independently. Because of this, the scan region between the contour and fill as well as the fill scan itself should be optimized.

It is important to note that the results of this study are not necessarily representative of all component designs and geometries fabricated by the machine. Extreme features, such as overhanging surfaces, fixed-free high aspect-ratio cantilevers, and thin walls are likely to exhibit sub-optimal properties and should be treated as such during the design phase.

2.4 Recommendations

From the results of this study, the necessity for additional verification and optimization studies is quite clear. Additionally, the results raise additional concerns about the performance of SLM-produced material. This section outlines the path forward for investigating these concerns.

2.4.1 Default Parameter Optimization Study

The SLM 125 HL is currently producing sub-optimal parts with significant edge porosity and inter-layer delamination. The goal of this proposed study is to improve the density of the components produced by the SLM 125 HL at Cal Poly through the optimization of its laser parameters and scan strategies. The following questions and

obstacles, many of which are likely to be covered in existing literature, must be addressed to achieve this goal:

2.4.1.1 Edge Porosity Questions and Obstacles

- What is the formation mechanism for edge porosity?
- How will Cal Poly measure and quantify edge porosity with its available resources?
- Is edge porosity consistent across different parameter suites (stripe, chess) and component designs?
- Can edge porosity be reduced through adjustments to the laser parameters and scan strategies?

2.4.1.2 Delamination Questions and Obstacles

- What is the formation mechanism for delamination porosity?
- How will Cal Poly measure and quantify delamination porosity with its available resources?
- Is delamination porosity consistent across different parameter suites (stripe, chess) and component designs?
- Can delamination porosity be reduced through adjustments to the laser parameters and scan strategies?

2.4.1.3 Suggested Learning and Resources

The following preliminary resources and learning objectives are recommended for researchers who wish to tackle this problem:

- A general understanding of the SLM 125 HL hardware and related software, such as the idea-to-print process and the post-processing techniques

- Complete comprehension of the laser parameters and scan strategies as is outlined in the Build Processor Manual
- Basic knowledge of density analytical techniques, cross-sectioning methods, and high magnification instrumentation

2.4.2 Expanding the Baseline Property Information Database

A database of baseline property information available for reference is useful when researching a novel process. However, as the SLM 125 HL is currently producing sub-optimal parts, it would be unproductive to build a body of analytical information only for it to be made obsolete by subsequent process improvements. For this reason, the study should focus on useful attributes that are largely independent of the laser parameters and scan strategies.

2.4.2.1 Powder Morphology and Size Distribution

The morphology and size distribution of a powder influences its flowability and performance in the SLM process. Although feedstock powder is provided with specifications from the vendor, it would do no harm to verify the documentation with particle size distribution and morphological analysis. To achieve this, researchers may use the Diary Science Beckman Coulter LS230 Particle Size Analyzer and the Materials Engineering a FEI Quanta 200 Scanning Electron Microscope.

Additionally, published literature lacks information on the size distribution and morphology of oversized particles removed from the feedstock during sieving operations. Analyzing this material may provide additional insight on the formation mechanisms of defects and potentially serve as additional indicator of overall build quality. As with the

feedstock powder, the same analytical techniques may be used to analyze the particles' properties.

2.4.2.2 Microstructural Analysis In Various States

Resource limitations impeded a thorough microstructural verification study for this body of work. Metallographic analysis of the 70 um – 1000 um characteristic length weld microstructures is necessary. Additionally, microstructural analysis of fully annealed SLM material may provide insight for future mechanical studies involving the heat treatment. Both of these efforts would require the use of an etchant more suitable than the electrolytic oxalic etch used in this study.

2.4.3 The SLM Microstructure and Sigma Phase Precipitation

The high energy sub-structure produced by the SLM process may influence the parent alloy's (316L) susceptibility to sigma-phase precipitation. The goal of this proposed study is to evaluate the effect of the SLM microstructure on sigma-phase precipitation. In summary, sigma-phase is known to precipitate at temperatures between 600°C and 1000°C. Studies show the fastest rates between 700°C and 810°C, with appreciable formation on the order of 100's of hours (Aydogdu & Aydinol, 2006). A side-by-side furnace comparison of wrought 316L and SLM 316L material with metallographic analysis may be sufficient to investigate the effect of the SLM microstructure.

3 LLNL Thin-Disk Component Failure Analysis

In August 2016, LLNL identified a thin hollow disk component (THDC) that had proven difficult to fabricate on their ConceptLaser M2 machines. An unknown number of attempts had built successfully but failed subsequent leak-proof tests over the period of at least 3 months. The organization suggested building a scaled-down version of the component on Cal Poly's SLM 125 HL, as a different machine architecture and fresh perspective could provide a useful path forward for successful fabrication. Detailed THDC design information and hardware that had failed the leak test were requested for analysis to determine the root cause and area of focus for the fabrication study.

In February 2017, LLNL released 3 defective THDCs, denoted Part #1, Part #2, and Part #4, to Cal Poly for non-destructive evaluation. Much of the information about the component design, such as its application, exact dimensions, fabrication plan, and test history, was not released. Additionally, delays in the setup of the machine and numerous logistical roadblocks obstructed the initialization of the fabrication study. As part of a significant scope reduction, a basic failure analysis study was performed on each released component. Based on the proposed root cause, a path forward for successful fabrication is provided.

3.1 Component Design and Print Information

As the original schematics and engineering drawings of the THDC are unavailable, all design information about the component was obtained through word-of-mouth or empirical measurements of the released hardware. The component was described by LLNL engineers as a hollow disk consisting of two 175 mm diameter circular walls of 0.5 mm thickness joined by a 6.35 mm wide cylindrical wall of unknown thickness. Two

6.35 mm tubes of 1.5875 mm thickness protrude 9.525 mm from the cylindrical wall to provide a fluid pathway through the disk's internal cavity (Figure 18). Small 3-legged struts span from one circular wall to the other in a square-grid pattern on the order of a few centimeters (Figure 19).

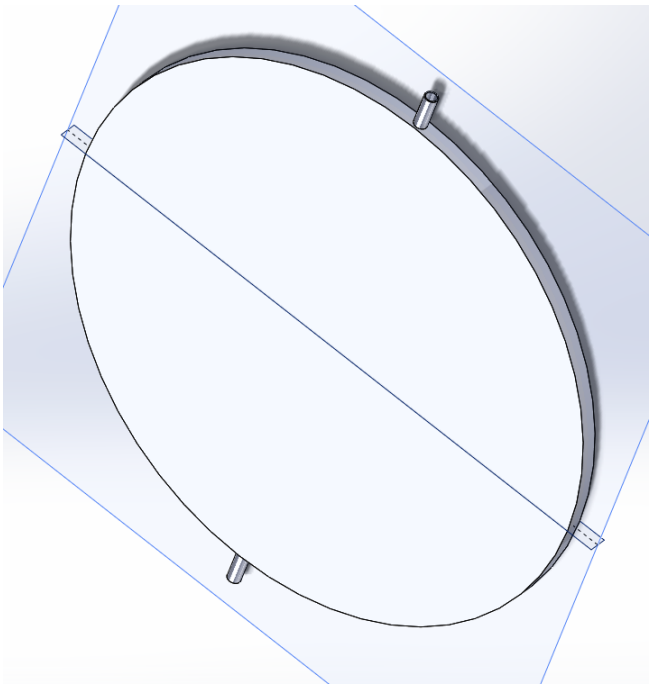

Figure 18. Mock-up CAD image of the exterior of the THDC.

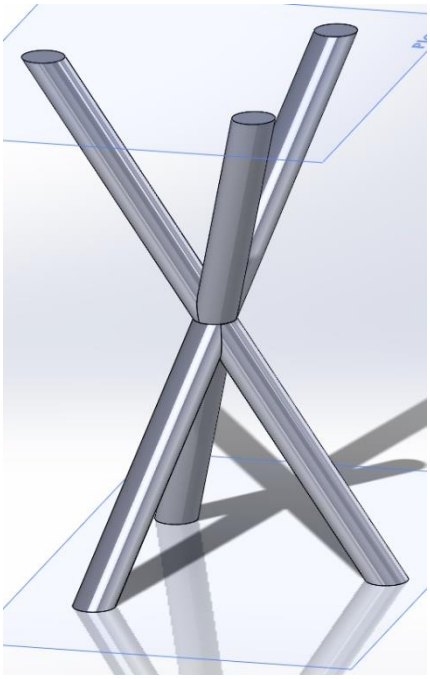

Figure 19. Mock-up CAD image of the internal 3-legged struts that span from one cylindrical wall to the other.

The orientation of the hardware during fabrication can be approximated from the remnant support structures observed in Section 3.2. All three released THDCs have the same support structure or support structure remnants and are assumed to have been printed in the same orientation. The components were built with their 2 circular walls perpendicular to the build plate. Support structures were generated on the downward facing cylindrical surfaces up to a 45° overhanging angle (Figure 20). It is assumed that there are no support structures on the internal side of the upward facing cylindrical surfaces, as these would interfere with the overall fluid flow of the component.

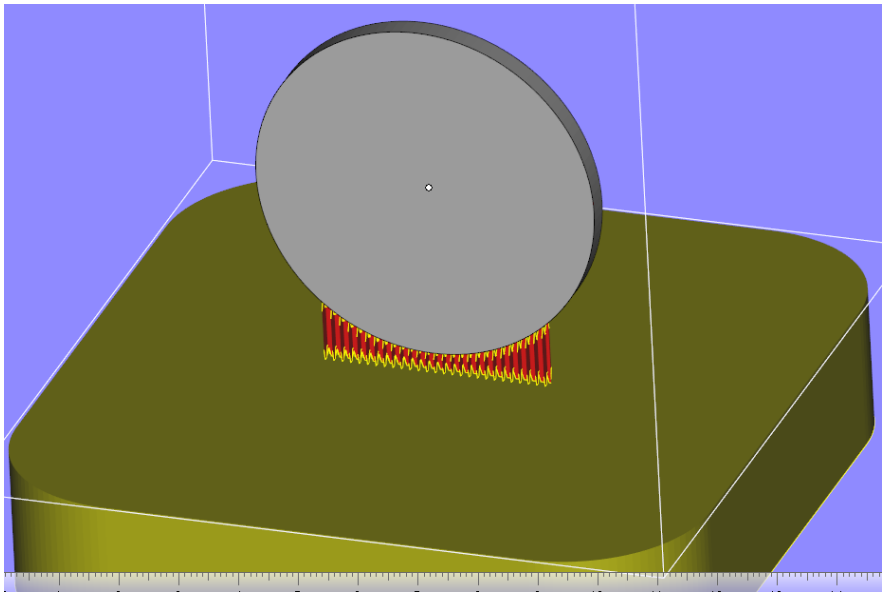

Figure 20. CAD model of the LLNL thin-disk component with support structures depicted in red and yellow. The orientation results in overhanging surfaces along the top and bottom sides of the cylindrical wall.

3.2 Visual Inspection

Part #1 and Part #2 share a similar appearance. The circular walls are uniform in appearance, with rough, light gray surfaces and mild parallel bumps running parallel to the build Z-axis. The cylindrical walls show dark coarsening along their mid-width that grows more apparent as the overhang angle relative to the build plate decreases. Part #1 still has its entire support structure attached (Figure 21), while Part #2 exhibits a smooth, machined surface where the original support structure interfaced with the component (Figure 22).

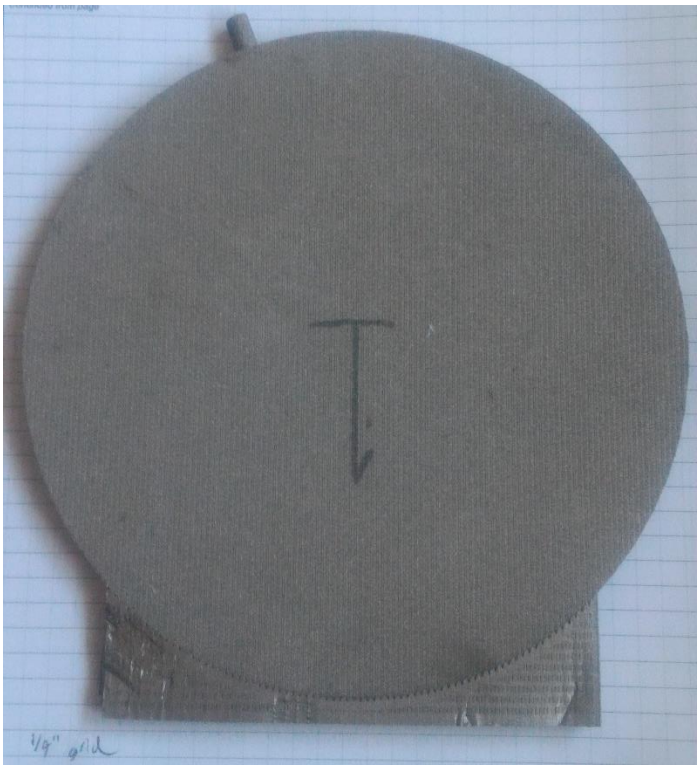

Figure 21. As-received image of Part #1. The orignial support structures are still attached to the downward facing section of the cylindrical wall.

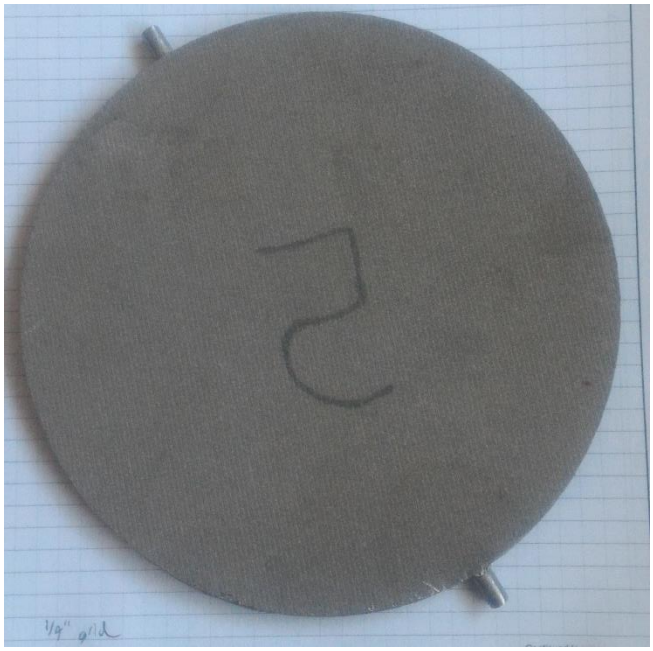

Figure 22. As-received image of Part #2.The support structures were removed by unknown means before the part was sent to Cal Poly.

Part #4 differs significantly in appearance. The uniform circular walls are smoother with a darker gray coloration and the bumps parallel to the Z-axis are much more distinct (Figure 23). The cylindrical walls exhibit less bumps, making the polygonization of the surface much more apparent. Scratches parallel to the XY-plane of printing of varying length, depth, and location mar one of the circular faces of the component. With the available information, it is difficult to determine if the scratches manifested during the SLM process or sometime during post-processing.

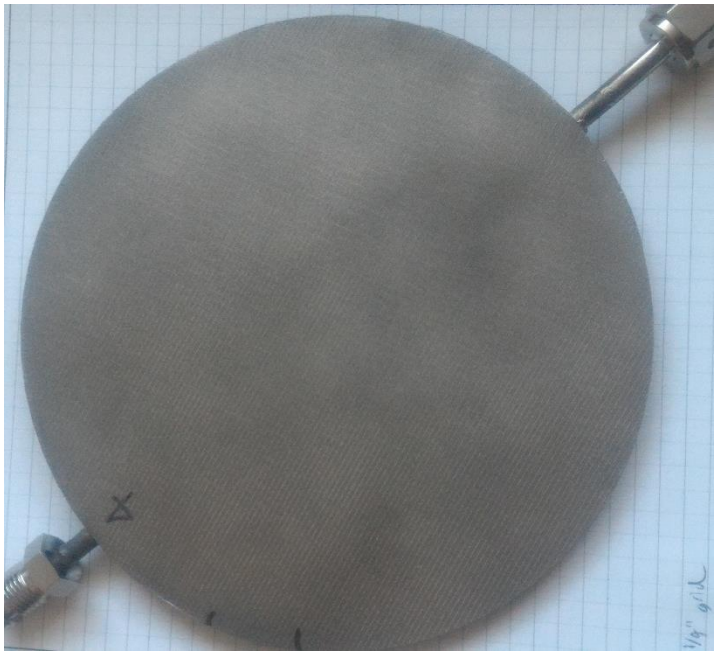

Figure 23. As-received image of Part #4. Adapters were welded to the tube openings before the part was sent to Cal Poly, presumably for leak testing.

Visual inspection suggests Part #1 and Part #2 were built in a similar fashion, while Part #4 had different fabrication conditions (Figure 24). This may be the result of differing feedstocks, altered processing parameters, dissimilar post-processing steps, or an unknown combination of each. Due to limitations imposed by the lack of processing information, it would be misleading to speculate any further.

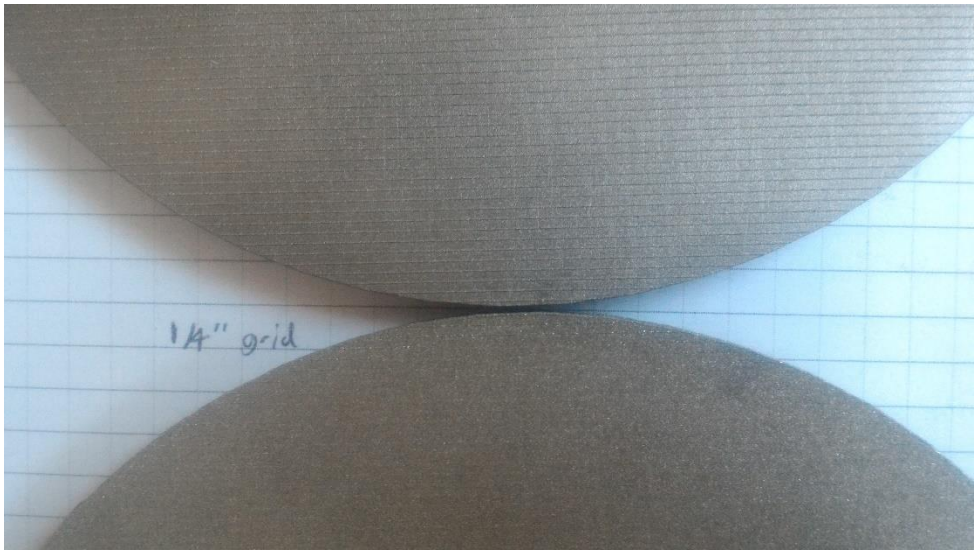

Figure 24. Side-by-side visual comparison of Part #4 (top) and part #2 (bottom).

3.3 Compositional Makeup Through X-Ray Fluorescence

All three disks were analyzed with Innov-X Systems X-ray fluorescence (XRF) gun on standard power and sensitivity settings. Part #1 and #2 had similar compositions within specifications of 316L. Conversely, the molybdenum content of Part #4 is above the 3.00% specification (Table 4).

Table 4. THDC XRF Results

Element	316L Specification	Part #1	Part #2	Part #4
Fe	Balance	66.38%	66.96%	66.55%
Cr	16.0% – 18.0%	17.33%	17.27%	16.65%
Ni	10.0% – 14.0%	10.60%	10.62%	10.85%
Mn	<2.0%	1.39%	1.47%	1.17%
Mo	2.00% – 3.00%	2.92%	2.88%	3.11%

All elements have an effect on the microstructure of the final part, especially with the rapidly liquating and solidifying SLM process. Molybdenum is a ferrite stabilizing element, meaning higher amounts of it will result in a higher delta-ferrite content. This can have a detrimental effect on corrosion susceptibility (Institute, 1988). Molybdenum

also promotes the formation and stability of the embrittling sigma phase, which can lead to a reduction in the ductility of the overall component.

Based on the available information, there is no indication of what caused the compositional difference in Part #4. Possible causes include feedstock compositional differences or altered processing conditions. If the feedstock compositional log for Part #4 is within specification, the results of this analysis serve as a compelling argument to perform post-fabrication compositional analysis on all future builds. This is especially the case when experimenting with different processing parameters, as is likely the case with Part #4.

3.4 Basic Overpressure Leak Testing

A basic leak test was conducted to locate the general spatial distribution of through-thickness leaks in the released THDCs. The components were covered with a mild soap solution formulated for maximum bubble production. The internal chambers of the THDCs were then pressurized with a 100 psi air pump and visually observed for bubble formation, location, and intensity.

Part #1 and Part #2 exhibit significant bubble formation along the mid-width of the cylindrical walls where the overhanging angle is less than 75° (Figure 25). This includes both the upward facing surface and the downward facing surfaces interfacing with support structures. This spatially correlates with the dark, coarse regions observed in Section 3.2 (Figure 26). No bubbles were observed on the circular walls of either component.

This aligns with the well-known limitations of the SLM process, as overhanging surfaces with angles less than 45° to the build plate must be sufficiently supported by

underlying structures. The presence of leaks along the support structure interface indicates an inadequate geometry that requires optimization for this application.

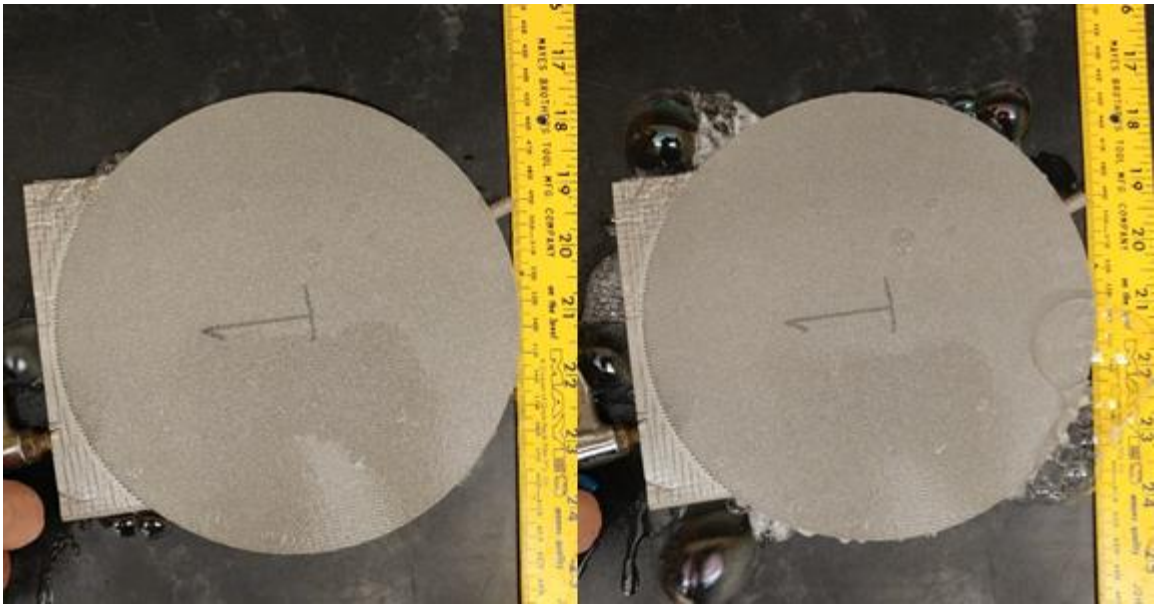

Figure 25. Soap-covered Disk #1 before and after air-pump induced internal pressurization.

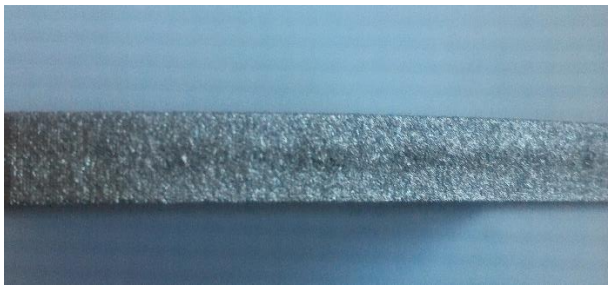

Figure 26. Mid-width dark coarsening on the upper cylindrical wall of Part #1.

Disk #4 exhibited a less pronounced bubble formation along one side of its upward facing cylindrical wall (Figure 27). The rest of its overhanging surfaces did not exhibit any bubbles. This may indicate that the single overhanging surface leak did not have the same formation mechanism as the overhanging surface leaks of Part #1 and Part #2, as it lacks the consistency across all overhanging surfaces and the correlated visual appearance.

Figure 27. Location of bubble formation on Part #4. The surface lacks any visual indication of defects in the form of through-thickness channels.

Additionally, bubbles developed from the deepest single scratch on the circular wall (Figure 28). As was stated in Section 3.2, the cause of the scratches cannot be determined with the available information. However, the leak results show that the scratches have a detrimental effect on the airtightness of the component, indicating that the scratch forming mechanism must be addressed in future builds.

Figure 28. Bubble-forming scratch on the circular wall of Part #4.

3.5 Proposed Mode of Failure

Based on the results of the basic leak test and accompanying visual inspection, there is sufficient evidence to conclude that incomplete through-thickness solidification of the overhanging surfaces is the primary mode of leak-proof failure for Part #1 and Part #2. Conversely, the results of the basic leak test and accompanying visual inspection are not sufficient evidence to conclude that Part #4 had the same primary failure mode as

Part #1 and Part #2. While the location of major Part #4 leaks has been determined, the root cause cannot be assessed without additional information. The mode of failure for Part #4 remains inconclusive.

3.6 Recommendations

Since the primary failure mode of Part #1 and Part #2 is a well-known SLM issue, some mitigation techniques already exist. This section proposes a path forward towards a fully solid, leak-proof pressure vessel through adjustments to the external support structures, the design itself, or the parameter suite. The pathway that fits best within the constraints of the application may be investigated by a follow-up researcher.

3.6.1 Additional Support Structures

It is likely that the proportion of support-to-surface contact has a considerable effect on the development of through-thickness leaks. The geometry of the support structure must be optimized for this application and is likely to include increasing the interfacing area. Once this is completed, the coverage of external support structures should be increased to include overhanging surfaces angles up to 90° relative to the build plate on the lower-half of the cylindrical wall. Note that this is not a full solution – the upper half of the cylindrical wall section cannot utilize support structures without interfering with the internal cavity geometry.

3.6.2 Design Modifications

Relatively minor design modifications can significantly increase the chance of a successful build for the THDC. However, the operating constraints are unavailable, making targeted recommendations difficult to identify. For this reason, a variety of general solutions are provided.

3.6.2.1 Preemptive Design Screening

As a preemptive measure, all parts proposed for SLM fabrication should be screened by a trained operator for fabrication-related issues. Specific to the THDC, the need for the upright orientation and the risks associated with the resulting thin-walled overhanging cylindrical surface can be identified early on and addressed before wasting build time and resources on attempts destined to fail. To facilitate this process, a general checklist could be maintained and shared between trained SLM operators.

3.6.2.2 Internal Braces

Adding internal braces that extend from the vertical circular faces to the overhanging cylindrical wall surfaces effectively acts as support structures without significantly altering the internal cavity geometry (Figure 29). The braces must be at least 45° from the build plate and may change in diameter and axial orientation to completely eliminate all overhanging surfaces, similar to the members of the IME Strut Card Holder Memento (5.10). This modification is only valid on the upward facing cylindrical wall and should therefore be accompanied with additional support structures as described in Section 3.6.1.

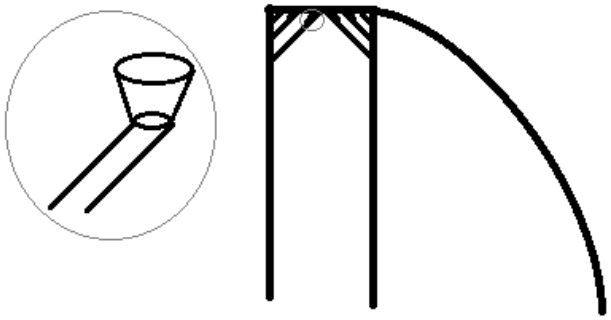

Figure 29. Additional support braces embedded in the upper section of the disk. The braces increase in diameter and coalesce at the outer wall, eliminating all overhanging surfaces less than 45° relative to the build plate from the cylindrical wall.

3.6.2.3 Contoured Interior

The internal corners of the cylindrical wall may be filleted to minimize the overhanging surface width to less than 1.0 mm, the minimum unsupported length when generating default block-type support structures (Figure 30). This design modification is only necessary along the upward facing section of the cylindrical wall. However, the entire cylindrical interior may be modified to maintain symmetry and the center of gravity of the component, as the vertical and downward facing sections are unlikely to be adversely affected by the change.

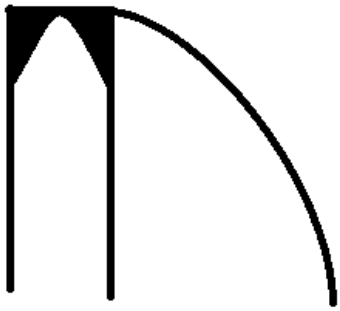

Figure 30. A fillet modification results in gradually sloping internal walls and a reduction of overhanging surface area.

3.6.3 Parameter Suite

In general, literature addresses overhanging surface and thin-walled feature improvement separately, with reduced surface roughness and increased structural integrity the measures of success, respectively. When the circular walls are oriented perpendicular to the build plate surface, the cylindrical walls are both overhanging surfaces and thin-walled structures. Therefore, the goal of the parameter optimization is to produce a fully solid strip of unsupported metal in as few layers as possible.

In general, high aspect-ratio strips of unsupported metal will peel-off during fabrication due to thermal contraction. However, the cylindrical walls of the THDC are anchored to the circular walls and the initial support structures. For this reason, the parameter optimization must be performed with the actual component design and should not be substituted with simplified versions of the cylindrical wall. Detailed design information is essential for this task and must be available at the start of the optimization study.

4 Preliminary Nil Strength Fracture Surface Study

As SLM is a relatively novel process, many opportunities exist for the application of less common analytical techniques. To support this, the unique capabilities of Cal Poly were assessed, resulting in the identification of the Materials Engineering Gleeble 1500. Gleebles are a class of thermos-mechanical physical simulation and testing systems with countless applications in the high-temperature metal processing industry. One of the many tests the Gleeble can perform is the nil strength test. A conductive specimen is held under a light tensile load and rapidly joule heated to its temperature of liquation. Separation occurs once a continuous liquid interface is formed along the specimen's cross section. The temperature at separation is defined as the nil strength temperature and may be used alongside other high temperature analyses to assess the weldability of the material.

Of greater use to the SLM field of knowledge is the fracture surfaces revealed by the nil strength test. On heating, liquation will first occur at regions with effectively lower melting temperatures, such as grain boundaries. Thus, the fracture surface will generally reveal microstructural characteristics in 3D and provide insight beyond the capabilities of conventional metallography. This, in addition to the lack of nil strength fracture surface analysis of SLM-fabricated specimens published in literature, is reason enough to initiate a preliminary microstructural analysis study using the aforementioned analytical techniques.

4.1 Experimental Design and Procedure

The standard ¼ inch diameter, 2 inch length cylindrical nil strength specimen was modelled in Magics. 2 specimens, denoted Z-1 and Z-2, were printed with the length-wise axis parallel to the Z-direction. An additional specimen, denoted XY-1, was printed with the length-wise axis parallel to the XY plane for a total of 3 specimens. All specimens were supported with the default "Block" support structure type and printed with the stripe parameter set.

The print containing the z-specimens was interrupted on a layer outside the gage length, resulting in a slight offset delamination. As this was not expected to affect the nil strength test, the print was resumed and completed without further complications. The XY specimen exhibited slight peel-off and delamination from its support structure due to thermal warpage, but was otherwise straight enough for nil strength testing. The specimens were excised from the build plate with a water-cooled horizontal band saw and the remaining support structures were removed with a 120 grit sanding belt.

The nil strength test was performed on a Gleeble 1500. The specimens were placed in water-cooled copper jaws and loaded with 20 lb-f of tensile force. A high temperature thermocouple was capacitor-discharge welded near the mid-length of the specimen to monitor its temperature. The specimen was then joule heated at a rate of 200°C/sec to 1300°C. The temperature was then ramped at a slower rate of 1°C/sec until the specimen separated completely. The fracture surfaces were analyzed with a FEI Quanta 200 Scanning Electron Microscope.

4.2 Results and Discussion

The Z-1 specimen was ramped to 1400°C, the temperature limit, and brought back down at air-cooling rates without separation. The temperature limit was increased to 1500°C, resulting in separation at 1419°C. Z-2 and XY-1 successfully separated during the initial heating cycle at 1380°C and 1389°C, respectively (Table 5).

Table 5. Nil strength temperatures of the SLM specimens.

Specimen	Nil Strength Temperature (°C)	Heating Cycles
Z-1	1419	3
Z-2	1380	1
XY-1	1389	1

4.2.1 Z-Orientation Fracture Surfaces

The Z specimens both show alternating rows of raised and lowered grains corresponding to two layer thicknesses, resulting in a plowed field appearance (Figure 31). The width and direction of the rows corresponds to the expected weld-track width and laser scan strategy.

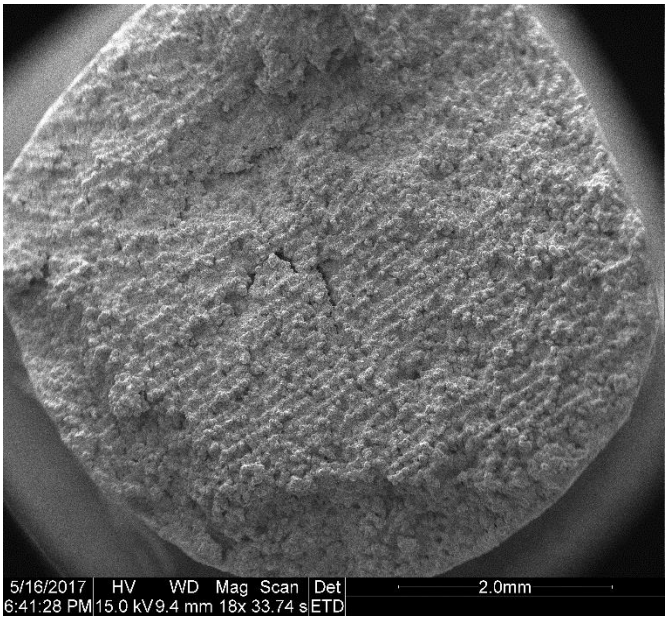

Figure 31. SEM image of the nil strength fracture surface of specimen Z-1. Rows of grains directly relate to the welds formed during the fabrication process.

The majority of the grains are between 20 um – 30 um in characteristic length. The surface of the grains exhibits a gnarled, bumpy appearance, thought to correspond to the cellular sub-structures seen in metallographic analysis, complimented with parallel layered stripes. The raised, lighter bumps are believed to be the higher-melting delta-ferrite phase alongside the darker, lower-melting austenite phase. The relative amounts of each of phase correspond well with observations made during metallographic analysis. EDS analysis would be able to compositionally verify this claim.

The layered stripes appear to run continuously though the grain, suggesting the layered sub-structure seen in metallographic analysis does not necessarily represent a perpendicular view of the cellular structure (Figure 32). However, it is unlikely that the stripes are lamellae similar to that of pearlite, as the diffusion required to form such a sub-structure requires a relatively slow cooling rate. Alternatively, the surface of the

grains may simply be solidification steps and minor agglomerates formed from the remnant liquid upon separation.

Most of the grain surfaces are rounded and globular, likely caused by partial melting resulting from the nil strength procedure. Occasionally, faceted grains resembling octahedrons are observed (Figure 33). This may be related to the plane systems of the FCC austenitic unit cell, of which crystals with facets cleaved along the closed-pack {111} planes resemble octahedrons in geometric shape.

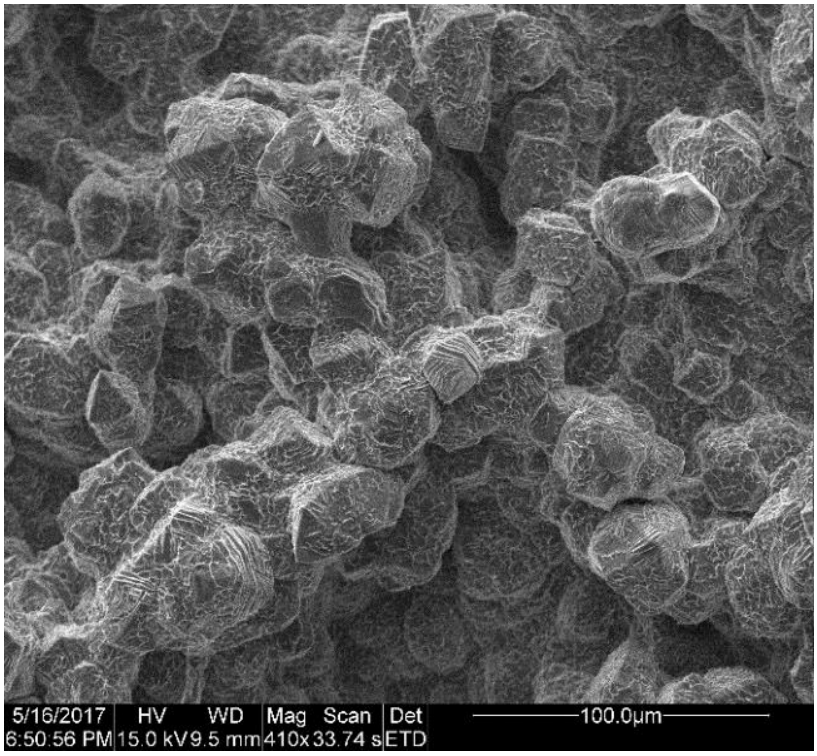

Figure 32. SEM image of two raised grain paths running from the bottom-left to the top-right on specimen Z-2. Gnarled, rough sub-structures neighbor lamellae.

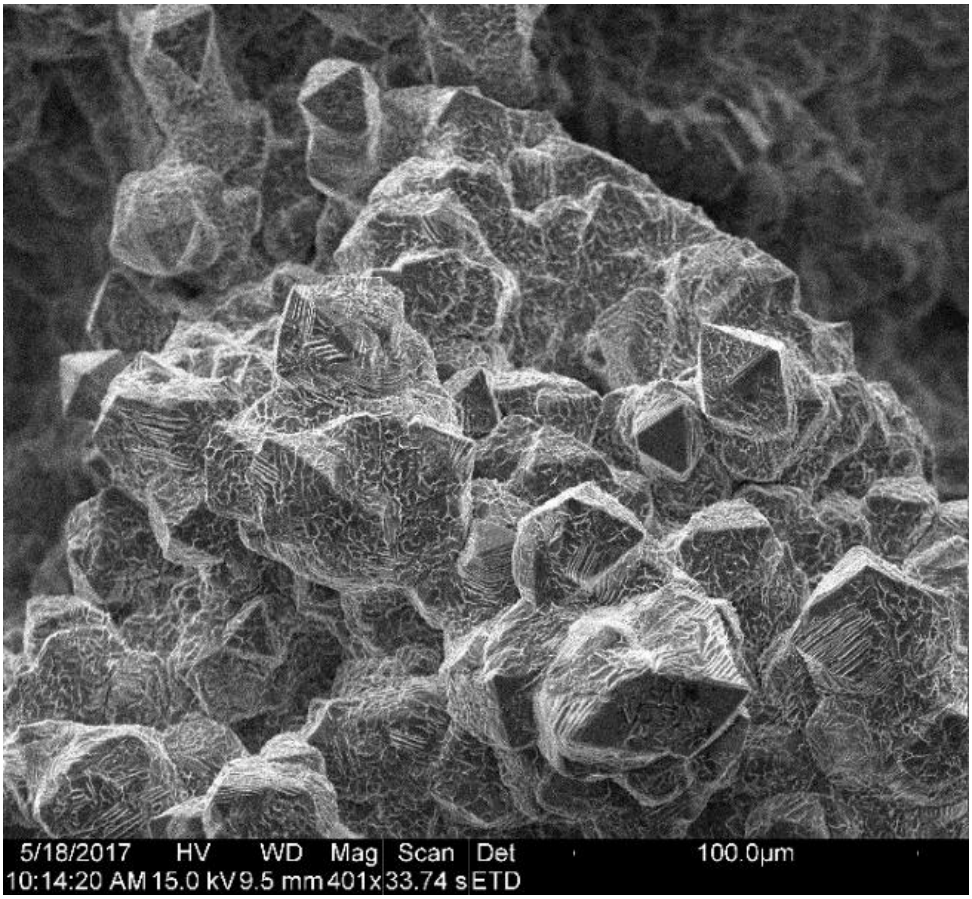

Figure 33. SEM image of rounded grains neighboring angular grains that closely resemble octahedrons. Specimen Z-2.

From the fracture surfaces, it is shown that preferential liquation first occurs between two layers. This suggest that a lower melting microstructural region, likely a semi-continuous grain boundary, is present at the interface of the mating layers. In the as-printed state, this is to be expected and reinforces the notion of anisotropy when comparing the Z-direction with the X or Y direction. This may be extended to fully annealed material should a heat treated nil strength specimen show a propensity for separation along its original layers.

4.2.2 XY-Orientation Fracture Surfaces

The XY-1 specimen exhibits texturing that roughly correspond to layers stacked upon each other (Figure 34). The texturing is not distinct enough to identify individual layers. This is not entirely unexpected, as literature shows each laser weld penetrates a couple layers at the deepest point in the melt pool. Columns of 5 – 10 distinct grains protrude from the surface (Figure 35). These structures may correspond with individual weld tracks that were bisected by the liquated surface of separation. Individual grains show the same substructures seen in the Z-orientation specimens (Figure 36, Figure 37).

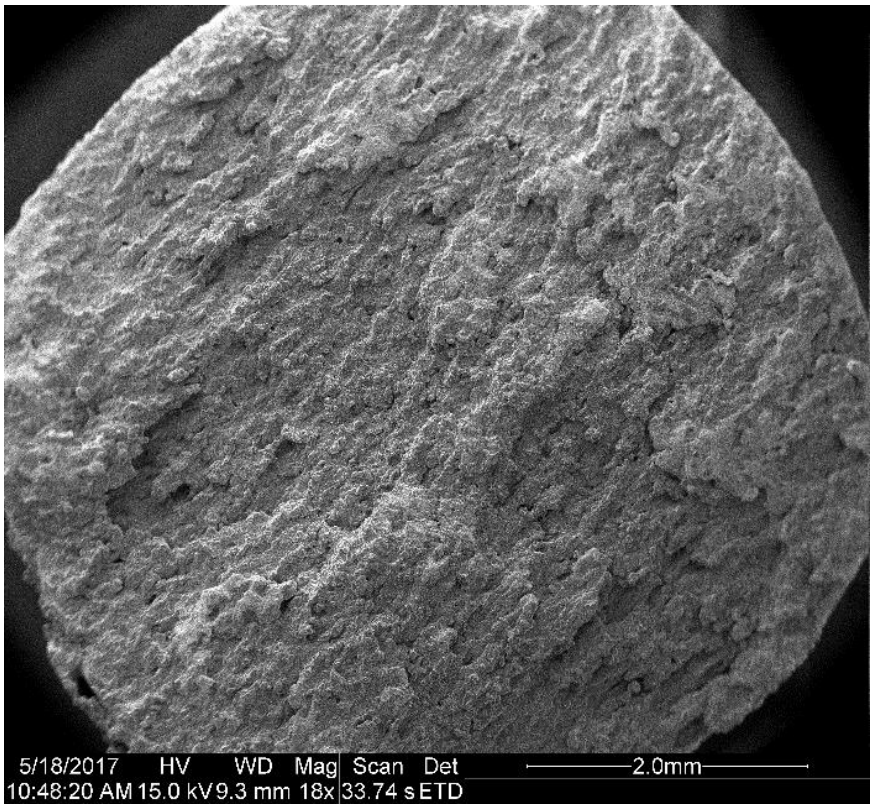

Figure 34. SEM image of the fracture surface of specimen XY-1.Rough layers lay parallel to each other, stacking from the bottom-right to the top-left of the image.

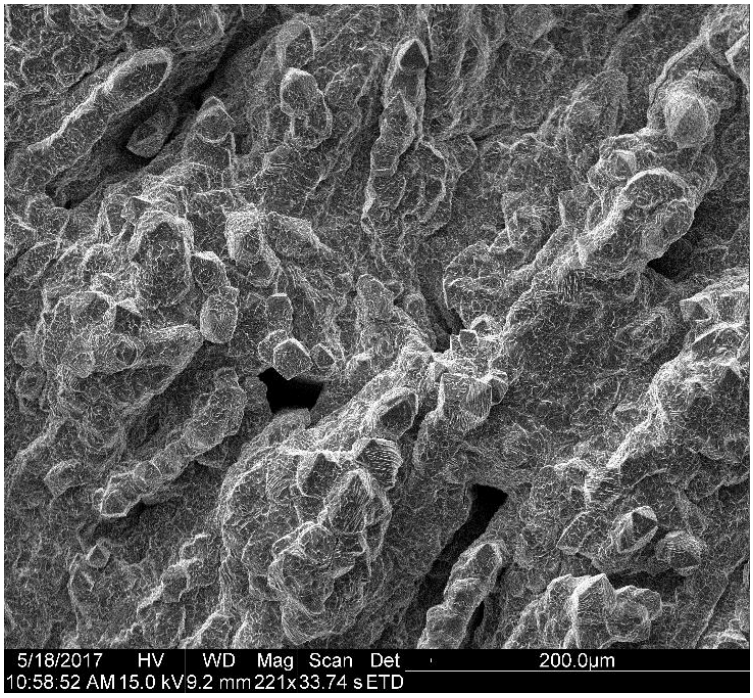

Figure 35. SEM image depicting small gaps between layers of specimen XY-1. Column-like clumps of grain protrude from the surface.

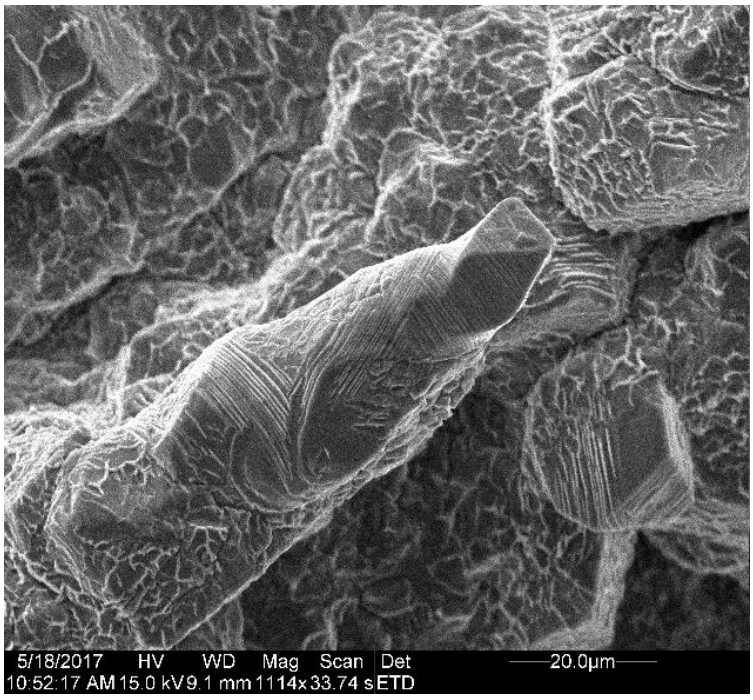

Figure 36. Single protruding column on specimen XY-1. Columnar sub-structures with varying orientations neighbor small, gnarled patches.

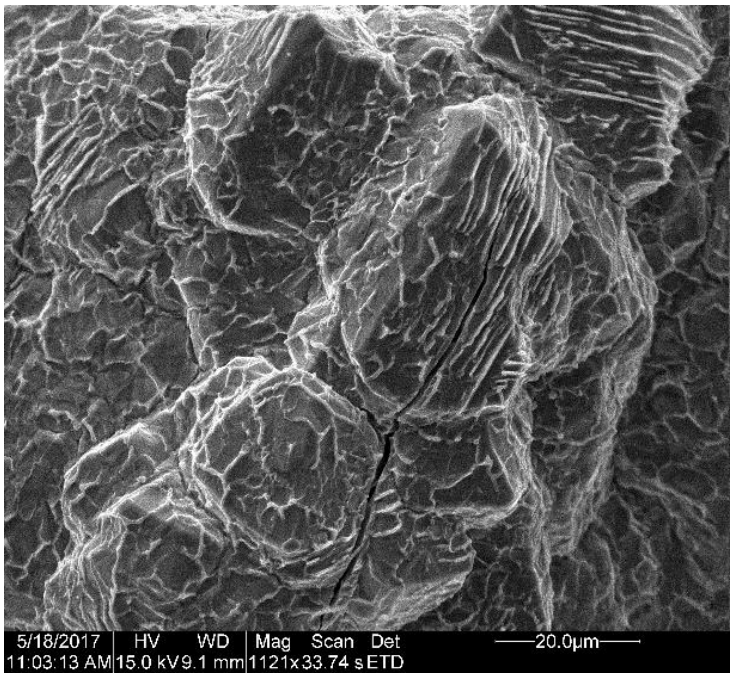

Figure 37. A crack on specimen XY-1 runs inter-granular at the bottom of the image to trans-granular at the top of the image, propagating between columns.

4.3 Conclusions and Future Work

A brief study was conducted to investigate the nil strength fracture surfaces of SLM-fabricated material as an alternative means of microstructural analysis. A propensity for initial continuous liquation between individual layers was observed. The individual grains exhibited gnarled, bumpy surfaces accompanied with columnar layers. These may correlate with the columnar sub-structures seen in metallography or be a result of resolidification during the nil strength process. Compositional analysis (EDS) of the gnarled regions is likely to shed light on the formation mechanism of these structures.

As a follow-up to this study, it is recommended to perform high temperature uniaxial compression testing as a means of inducing unusual microstructural phenomena with accompanying fracture surfaces, such as the strain-induced crack opening test. The study

would use smaller specimens (such as 10 mm in diameter and 15 mm in length) that are less prone to buckling.

It should be noted that the utility of such a study is primarily aesthetic. The high temperature thermo-mechanical properties of 316L stainless steel is well understood, and it is unlikely that components produced by the SLM process would be exposed to such extreme operating conditions or processes. Regardless, the importance of contributing to the general SLM body of knowledge and the potential for discovering new information cannot be understated.

5 Part Design Experimentation

A variety of parts were designed for the selective laser melting process to evaluate the capabilities of the SLM 125 HL (Table 6). Emphasis was placed on complex internal geometries, sharp edges, and variable overhanging surfaces. This section outlines the design philosophy, implementation, and lessons learned for each component. Unless otherwise stated, all parts were printed with the default chess parameter set, raised 5.0 mm above the build plate by support structures, and excised with a coolant-sprayed horizontal band saw without further post-processing or heat treatment.

Table 6. Summary of Test Components

Component	Main Features	Success?
Double Bell	Curves, Thin Overhanging Surfaces	Yes
Rings	Fine Features, Channels	No
HexaLoft	Complex Continuous Surfaces, Fine Features	Yes
TetraBall	Sharp Corners, 60° Overhanging Members	Yes
CubeBall	Sharp Corners, 45° Overhanging Members	No
Octahedrons	Sharp Corners, 45° Overhanging Bodies	No
Radial & Strut Mementos	Complex Continuous Surfaces, Fine Features	Yes
Lattice Cube	Thin 45° Members	No
Supermileage Coupler	Fine Tolerance, Complex Geometry	Partial
Golf Club Inserts	Internal Lattice, Complex	Unknown
“Crackhouse”	High Residual Stress Load	Yes
Support Structure Suite	Overhanging surfaces, Unusual .STL File	Yes

5.1 Mode-2 Double Bell

A double-layer 2” bell with a complex curvature, alternating overhanging surfaces, and an embedded subsection was modelled in SolidWorks for the SLM process. Inspired by a fixed-free cantilever, the bell was further influenced by classical bell aesthetics and curvature.

The design of the bell began with a SolidWorks frequency analysis of a basic rectangular cantilever (Figure 38). The 2nd natural frequency was analyzed for its relative anti-node and node position. The minor anti-node and unfixed node were determined to be 0.468L and 0.786L from the fixed side, respectively.

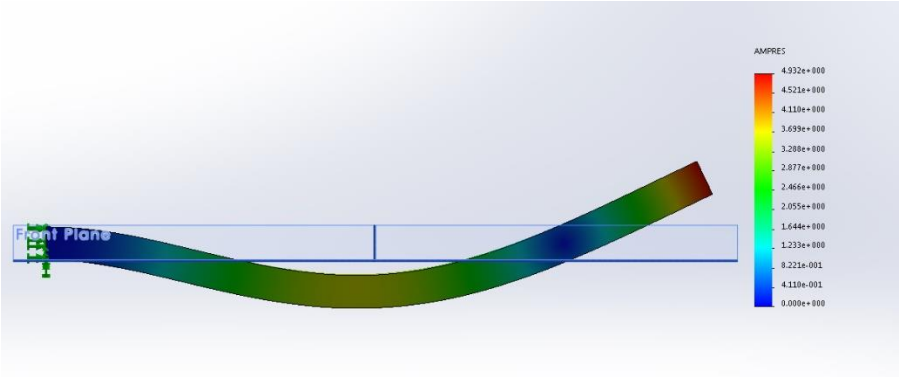

Figure 38. SolidWorks FEA simulation of the mode-2 resonant frequency of a fixed-free cantilever.

The bell wall was formed around the hypotenuse of a 30/60/90 triangle (W = 1”, H = 2”), chosen to enable minor curvature changes without approaching the 45° overhanging surface limit. 30° curves were drawn between the minor anti-node and node locations. The thickness was varied from a base-nominal of 0.05” at the head, decreasing to 0.025” at the anti-node (to reduce the effective stiffness and encourage deflection), increasing to 0.1” at the unfixed node (to decrease the rotational moment around this point and increase its stiffness, thereby discouraging deflection), and decreasing back to the base-nominal of 0.05” at the lip. FEA of the bell cross-section showed a strong propensity towards the desired 2nd natural frequency (Figure 39).

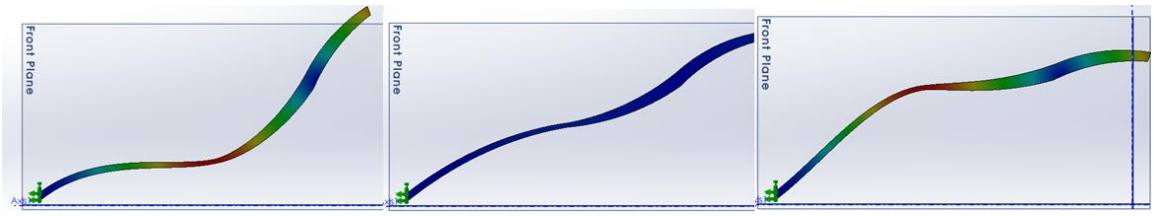

Figure 39. SolidWorks FEA simulation of the mode-2 resonant frequency of the outer-bell wall cross-section. The maximum deflecting section corresponding to the anti-node occurs at the thinnest thickness (red), while the relatively stationary section corresponding to the node occurs at the thickest thickness (blue).

A similar, second bell with half the thickness of the first was drawn using the hypotenuse of a 15/85/90 triangle (W = 0.5”, H = 2”). Both curves were attached at the head with a small rectangle to serve as a handle and revolved around the central axis to produce the 3D bell shape (Figure 40).

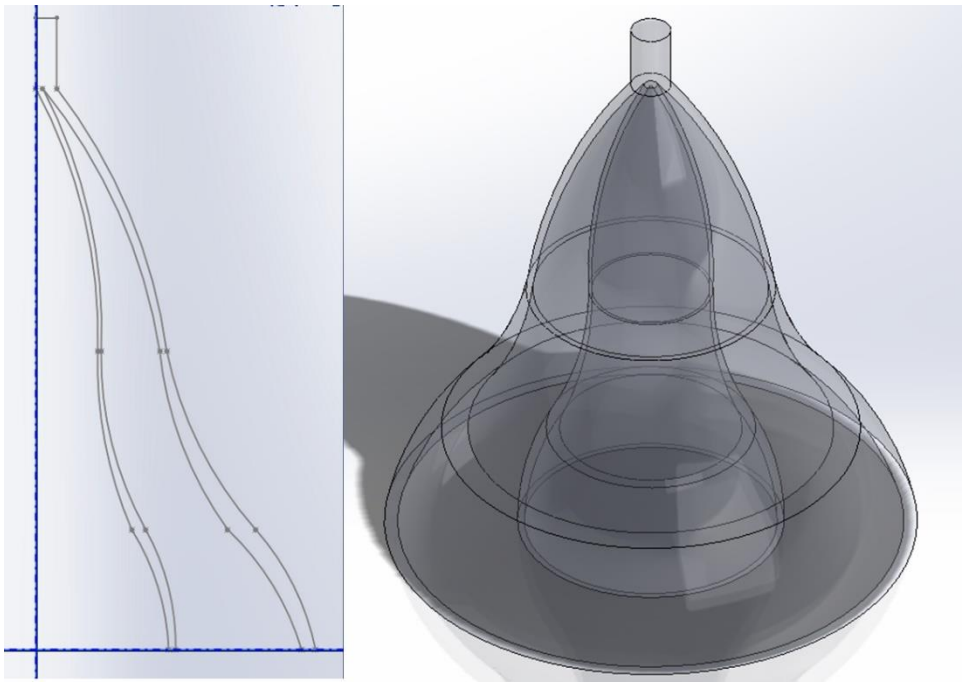

Figure 40. Cross-section and semi-transparent CAD image of the final double-bell.

5.1.1 Print Details

The base of the bell was aligned parallel to the build plate and raised up 5.0 mm with the default ‘line’ support structures (Figure 41). As was intended from the inception of the design, no additional support structures were required along the walls or head of the bell.

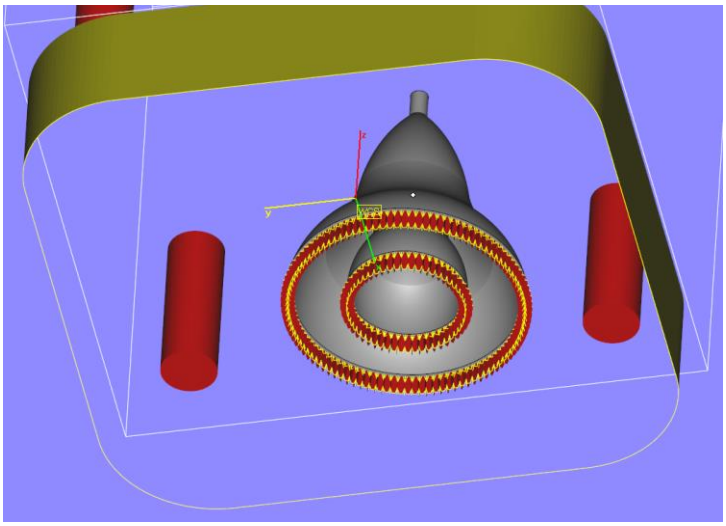

Figure 41. Double-bell and accompanying line-type support structures viewed from below the build plate in Magics.

The bell was printed without any complications originating from its design (Figure 42). Deviation from the original dimensions due to residual stress warpage was insignificant. The line-type support structures obstructed removal of the powder trapped inside the bells, necessitating the use of a hand-saw to release the powder.

Figure 42. As-printed bell. Minor polygonization from the .stl to .slm conversion process is visable on the surface of the outer bell.

The outer bell rings at 3967 Hz base frequency, with a 6858.33 Hz and 6949 Hz paired overtone, resulting in a modulated buzzing at initial strike followed by an extended high pitched ringing. The inner bell acts as a dampener to the outer bell's vibrations and fails to produce a significant tone when struck. For this reason, it was removed from the assembly and tested individually. The inner bell rings at 11516 Hz with numerous miscellaneous overtones.

5.1.2 Lessons Learned

The contour scan path produces a near-net surface finish without evidence of patterning originating from the internal chess scan strategy. This may be contrasted by the ConceptLaser machines at LLNL, which produces large linear patterning along vertical surfaces due to the chess pattern overlapping with the edges. The reduction of such milli-scale features and the affiliated stress risers is likely to result in overall superior mechanical properties.

The default line-type support structure prevents powder release while the part is still on the build plate. Depending on the design of the component, this may result in the waste of significant amounts of powder while posing a health and contamination hazard during build plate removal operations.

5.2 Axial Channel Rings

Numerous rings were modelled in SolidWorks to evaluate the dimensional tolerance of the SLM machine and the possibility of printing around the edges of the bolt mounting holes. Although the theoretical minimum resolution of the machine is rated at 140um, this varies depending on the type of geometries printed. Sharp angles, rounded surfaces, and differences in the XY vs Z direction can contribute to changes in the print resolution.

Two 0.75" outer diameter, 0.685" inner diameter, 0.25" wide base rings were printed with various through-width channels from one 0.0325" thick circular surface to the other (Figure 43). The first ring's channels consisted of the words "SIGHT UNSEEN" in Times New Roman, 1.0 mm tall font. The second ring's channels consisted of various astronomy signs from the Wingding 1.0 mm tall font pack. All letters and signs were selected to be absent of free floating segments (such as the floating D shape in the letter "P").

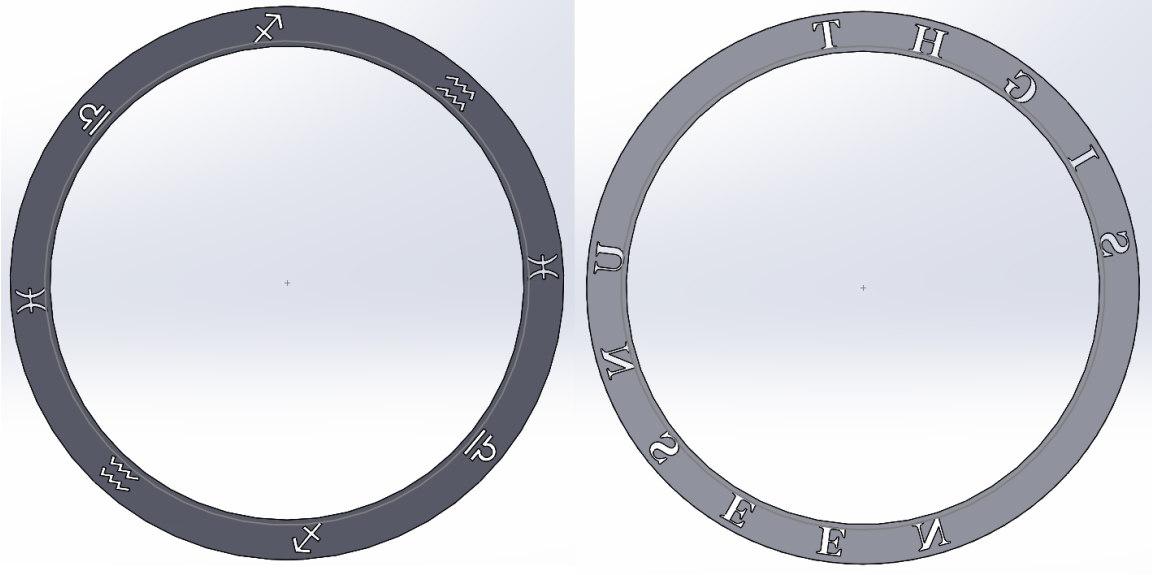

Figure 43. CAD image of Astronomy and "SIGHT UNSEEN" ring, viewed along the central axis.

5.2.1 Print Details

The 0.0325” faces were aligned parallel to the build plate and placed to encircle the bolt mounting holes (Figure 44). Both rings were supported with the Default line-type support structure type and were printed successfully without any design-related complications arising during the SLM process.

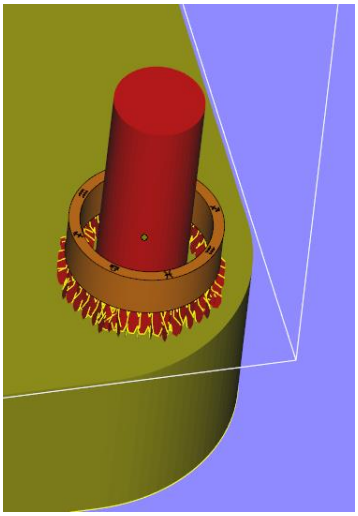

Figure 44. Astronomy ring with its central axis aligned with the stay-out region associated with the build plate screw holes. Line-type support structures depicted in red and yellow.

Both components exhibit a consistent surface finish with respect to layer count on the outer and inner ring surfaces. The channels of both rings show poor resolution with significant through-thickness obstruction (Figure 45). The astrology ring shows dark bands on its outer surface corresponding to each astrology channel, likely a result of the wall thickness between the channel and the outer ring surface reaching a critical minimum (Figure 46).

Figure 45.Top-down view of SIGHT UNSEEN (left) and Astrology (right) ring. Poor channel resolution obscures the through-thickness view.

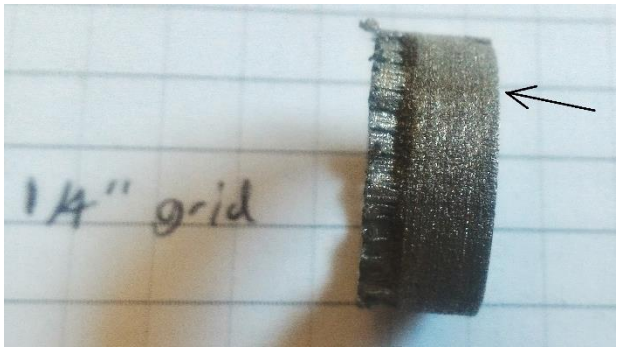

Figure 46. Dark bands on the outer wall of the Astrology ring.

5.2.2 Lessons Learned

Irregular wall thicknesses should be at least 0.5 mm for a consistent surface finish. This minimum should not be considered satisfactory for uniform thickness thin-wall

sections without further testing, as such components would have a high aspect ratio coupled with a geometry susceptible to buckling, putting it at risk for thermal warpage.

5.3 4-Chamfer Ring

A 0.85” outer diameter, 0.685” inner diameter, 6.0 mm wide base ring with a 1.15 mm deep 120° double chamfer along the mid-width and a two 2.0 mm tall 60° inner chamfers along each inner edge was modelled in SolidWorks as a follow up to the axial-cut out base ring (Figure 47). 16 alternating triangle channels run from the upper outer chamfer to upper inner chamfer. 16 alternating triangle channels run from the other outer chamfer to the accompanying outer face of the ring.

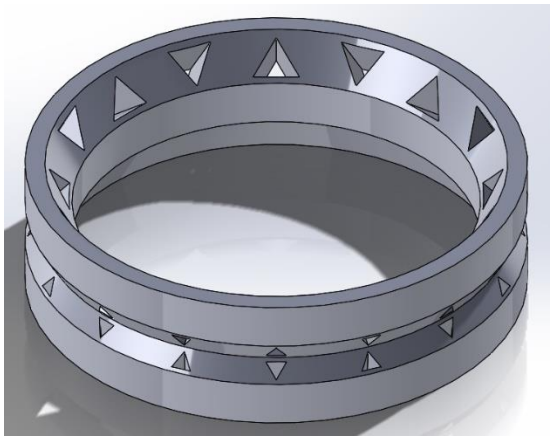

Figure 47. CAD image of the 4-Chamfer ring.

5.3.1 Print Details

When the outer face with alternating triangles is oriented to face the build plate in parallel, none of the internal features are less than 45° from the build plate (Figure 48). The ring was supported above the build plate with the default “contour” support structure type and was printed successfully without any design-related complications arising during the SLM process.

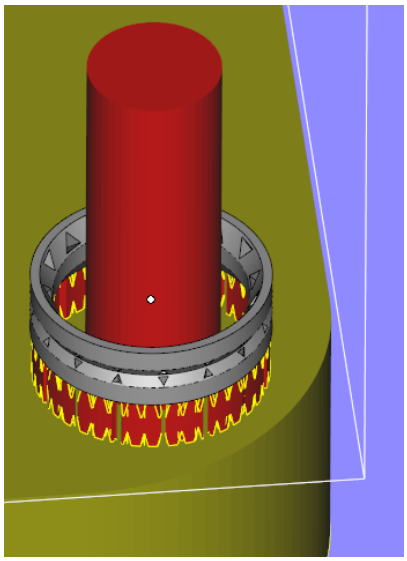

Figure 48. 4-chamfer ring with its central axis aligned with the stay-out region associated with the build plate screw holes. Contour-type support structures depicted in red and yellow.

The large 1.68 mm triangle channel openings on the upper inner chamfer exhibit excellent dimensional tolerance and aesthetics (Figure 49). Conversely, the 0.76 mm triangle channel openings on the outer chamfer hardly resemble triangles in shape. Both the downward-facing and upward-facing outer chamfer triangles have poor dimensional tolerance.

Figure 49. As-printed 4-chamfer ring. Upper triangle channels, while poor in geometrical resolution, are unobstructed their entire length.

5.4 HexaLoft

A 25.4 mm tall, 22.0 mm wide hexagonal tube with alternating overhangs, sharp edges, and a smooth transitionary outer surface was modelled in SolidWorks to evaluate the surface finish print quality of the SLM 125 HL (Figure 50). The tube varies from 0.5 mm to 2.0 mm in thickness along its length and features a clockwise rotating outer surface and a counter-clockwise inner surface. The top hexagonal face of the tube features the words “I DON’T HAVE ANYTHING TO SAY” in 0.95 mm tall Times New Roman debossed 0.5 mm into the surface.

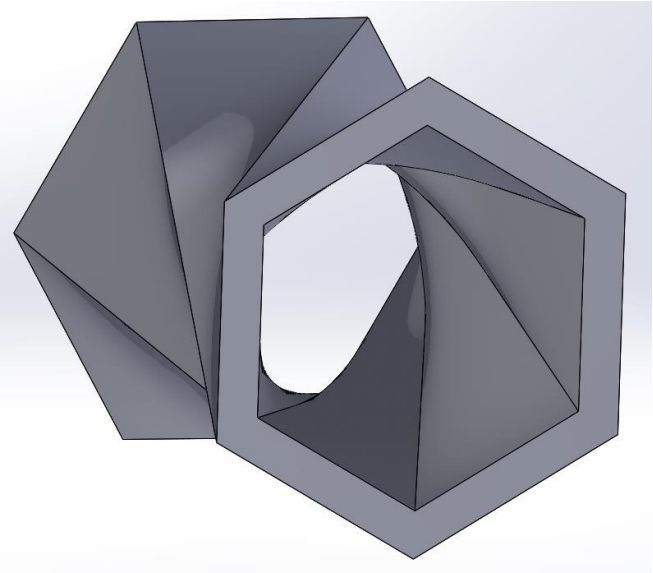

Figure 50. CAD image of the hexaloft. Outer and inner surfaces rotate in opposite directions by 90°.

5.4.1 Print Details

The lower hexagonal face was aligned parallel to the build plate. In this orientation, no additional support structures were necessary along the tube walls (Figure 51). The component was supported with the line-type support structure and was printed successfully without any design-related complications arising during the SLM process.

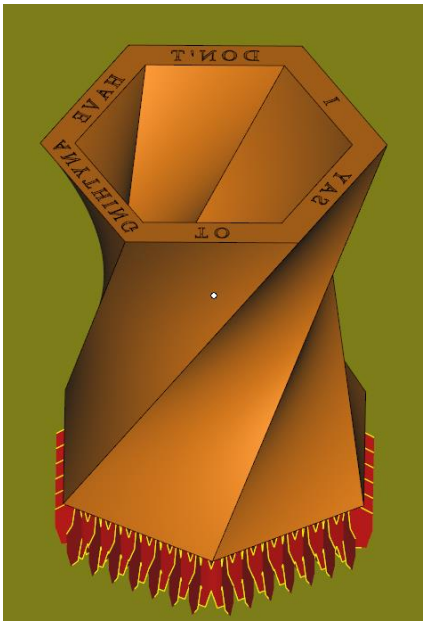

Figure 51. Hexaloft with the line-type support structure at its base.

The lofted hexagonal tube faces show consistent surface finishes independent of orientation or overhang angle. The mating longitudinal edge along the tube face are also uniform and stable. The lower hexagonal face mated with the line support structure shows significant burn-in and poor coherence (Figure 52). Only material within 0.5 mm of the support structure show appropriate solidification and surface finish. The debossed lettering on the upper hexagonal face show good dimensional tolerance. However, the interior debossed surface is inconsistent in depth. Close inspection reveals incompletely melted powder adhered to the surface. This is contrasted with standard upward facing surface geometries consisting of overlapping parallel weld tracks approximately 70 um in width.

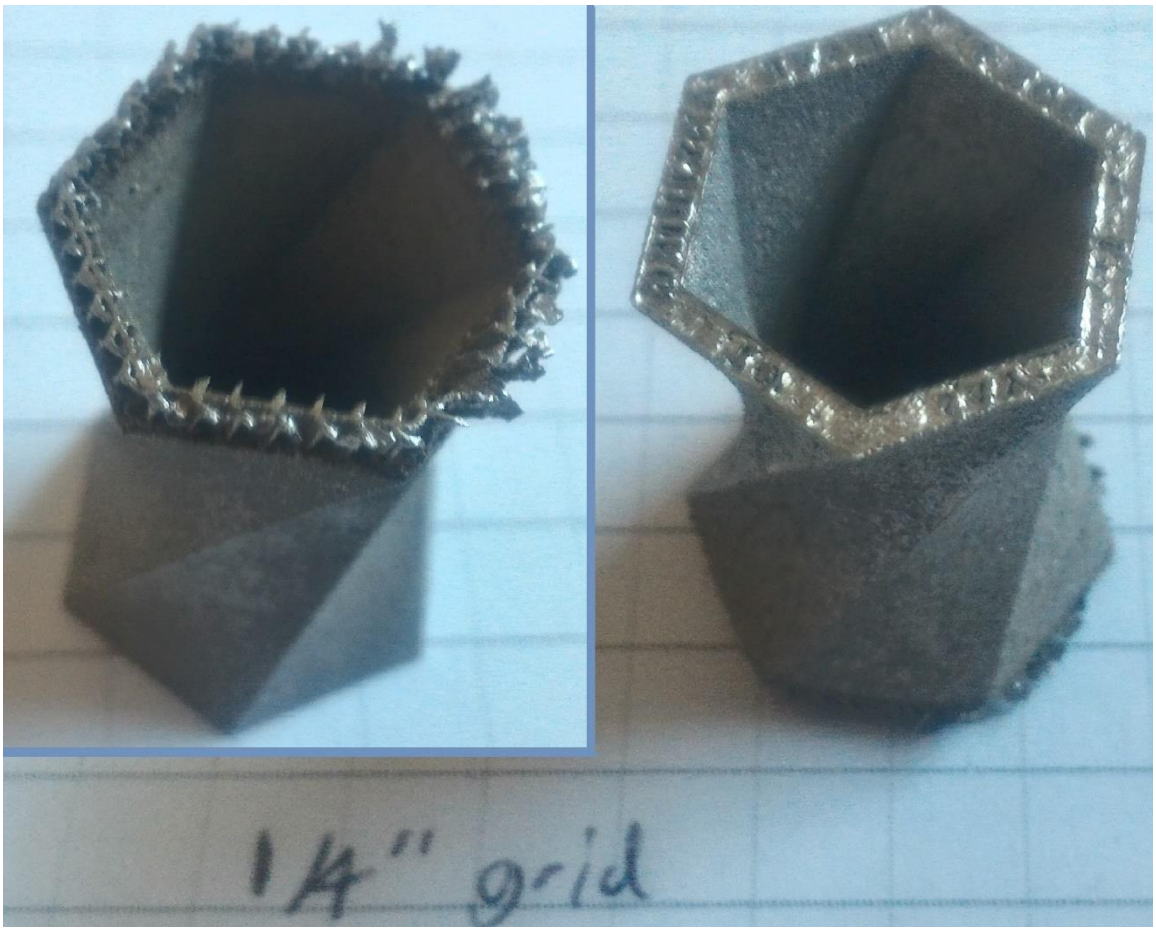

Figure 52. Bottom (left) and Top (right) view of the Hexaloft. Debossed lettering and unsupported downward facing surfaces show poor dimensional resolution.

5.4.2 Lessons Learned

The default line-type support structure inadequate for non-edge downward facing features. The appropriateness of contour, block, or the other untested support structure types depends on the downward face geometry (Figure 53). More information is provided in Section 1.1.6.

Upward facing surfaces surrounded by vertical walls may be prone to poor surface finish at tight dimensions. More specifically, the corner between an upward facing surface and a vertical wall should be expected to have surface defects. The resultant stress concentrations should be considered during design.

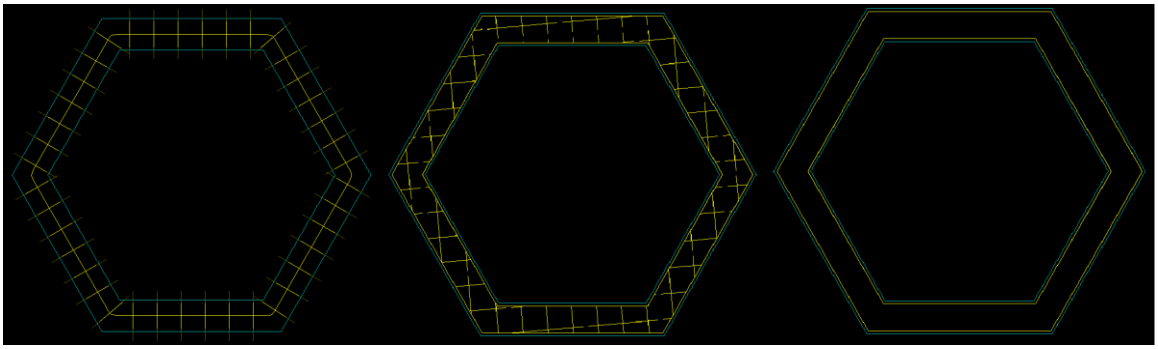

Figure 53. Line (left), block (center), and contour (right) support structures on the Hexaloft.

5.5 Tetrahedron with Caged Sphere

Polyhedrons are excellent test components due to their known, solvable geometries, consistent and patterned features, general symmetry, and sharp edges and corners. Thin-member polyhedrons were printed to demonstrate the SLM's capabilities while testing various overhanging surface angles and simple thin members.

A 20 mm tall tetrahedron composed of 2.0 mm tall triangular struts with a 0.7 mm diameter sphere caged in its center was modelled in SolidWorks to evaluate 60° overhanging surfaces, a sharp upward pointed feature, and the viability of trapping solid material in an internal cavity (Figure 54). The numbers 1 through 4 were debossed 0.3 mm into each corner of the tetrahedron akin to a 4-sided dice.

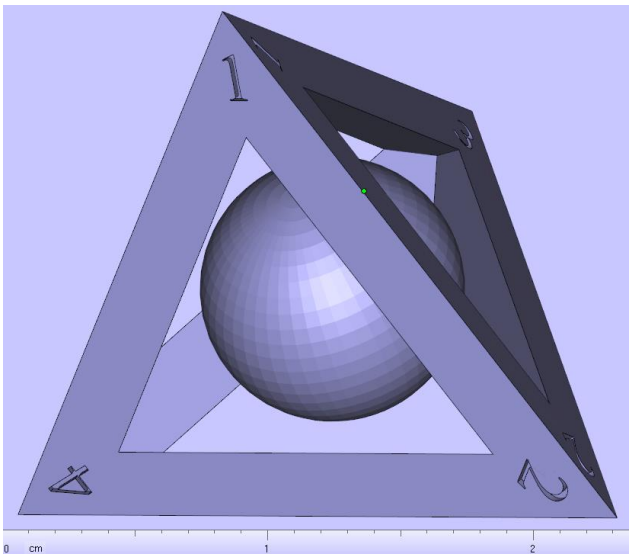

Figure 54. CAD image of the Tetrahedron with Caged Sphere. Debossed numbers detail each 3-member edge.

5.5.1 Print Details

The triangular face opposite to the corner labelled with the number "1" was aligned parallel to the build plate (Figure 55). In this orientation, a fraction of the debossed numbers was flagged as overhanging edges. The decision was made to override the default rules and to only generate supports on the downward facing triangular face and the caged sphere with the default "Block" support type. The debossed surfaces of the downward facing numbers were intentionally left unsupported. The part was printed successfully without any design-related complications arising during the SLM process.

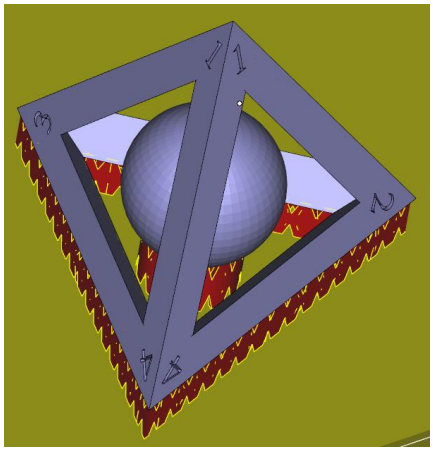

Figure 55. Tetrahedron and Caged Sphere attached to the "Block" type support structure.

All of the tetrahedron members printed successfully with a consistent surface finish (Figure 56). The sphere exhibits a minor increase in surface roughness on its overhanging surface near the edge of the support structure generation cut-off. All upward facing numbers are legible with minor dimensional deviations. The three downward facing numbers on the triangular face facing the build plate are faintly legible but exhibit poor surface finish.

Figure 56. Tetrahedron with Caged Sphere with its support structures removed.

5.6 Cube with Caged Sphere

A 20 mm edge-length cube consisting of 2.0 mm-wide square struts with an 18 mm diameter sphere caged in its center was modelled in SolidWorks to evaluate 45°

overhanging surfaces, high-aspect ratio beams, and sharp overhanging corners (Figure 57).

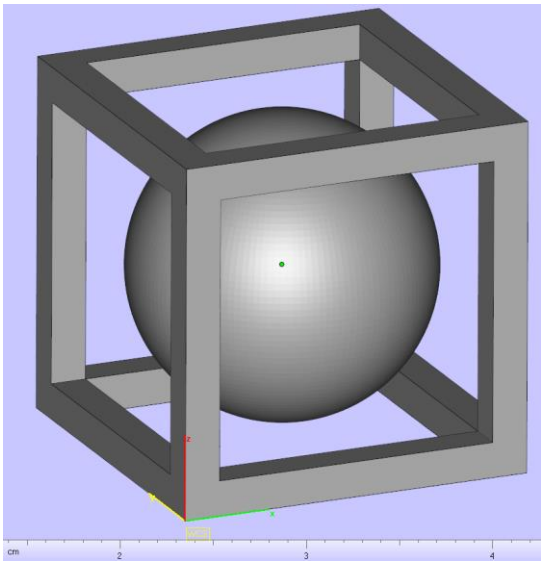

Figure 57. CAD image of the Cube with Caged Sphere component.

5.6.1 Print Details

The cube was oriented to balance on the build platform by one of its corners, minimizing the area of less than 45° overhanging surfaces (Figure 58). This necessitated generating support structures from the caged sphere downward surface, around the intersecting cube struts, and onto the build platform itself (Figure 59). A significant portion of the sphere could not be supported without modifying the strut geometry.

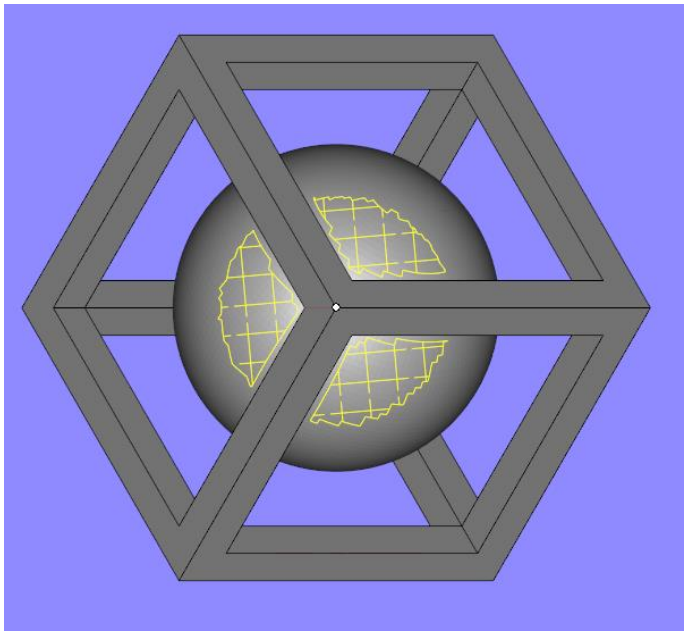

Figure 58. Underside view of the Cube with Caged Sphere component and its block-type support structure. The structures raise the sphere above the Cube and keep the two sub-sections independent.

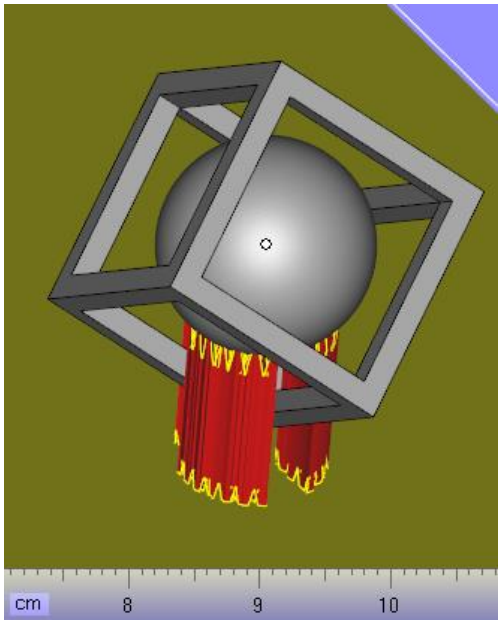

Figure 59. The Cube with Caged Sphere component on the build plate. The Cube is attached solely by a single corner surrounded by the Sphere support structures.

The SLM experienced significant difficulties printing the component. Due to the minimal anchoring contact between the cube struts and the build plate, the unconstrained

thermal expansion and shrinkage caused the high aspect ratio struts to raise at least 30 microns above the powder surface, resulting in significant damage to the recoater blade as it passed over during powder spreading operations. The damaged recoater blade failed to spread powder evenly for subsequent layers, resulting in a warped, bumpy appearance for the overall part (Figure 60).

Figure 60. As-printed Cube with Caged Sphere. The effect of poor dimensional resolution caused by early damage to the recoater is exhibited by the cube members.

5.6.2 Lessons Learned

High aspect ratio subsections that will be unevenly heated must be anchored to the build plate to prevent thermal warpage and subsequent damage to the recoater. From another perspective, if subsections are fabricated as fixed-free cantilevers during the SLM process, they must be anchored to the build plate.

5.7 Cut Octahedrons

A 1/2-cut and 7/8-cut excised 3.6 mm tall octahedron consisting of 3.5 mm thick trapezoidal struts was modelled in SolidWorks as a supplementary test component to the Cube with Caged Sphere (Figure 61). As with the cube, the purpose of the component is to evaluate 45° overhanging surfaces, high aspect ratio beams, and sharp overhanging corners.

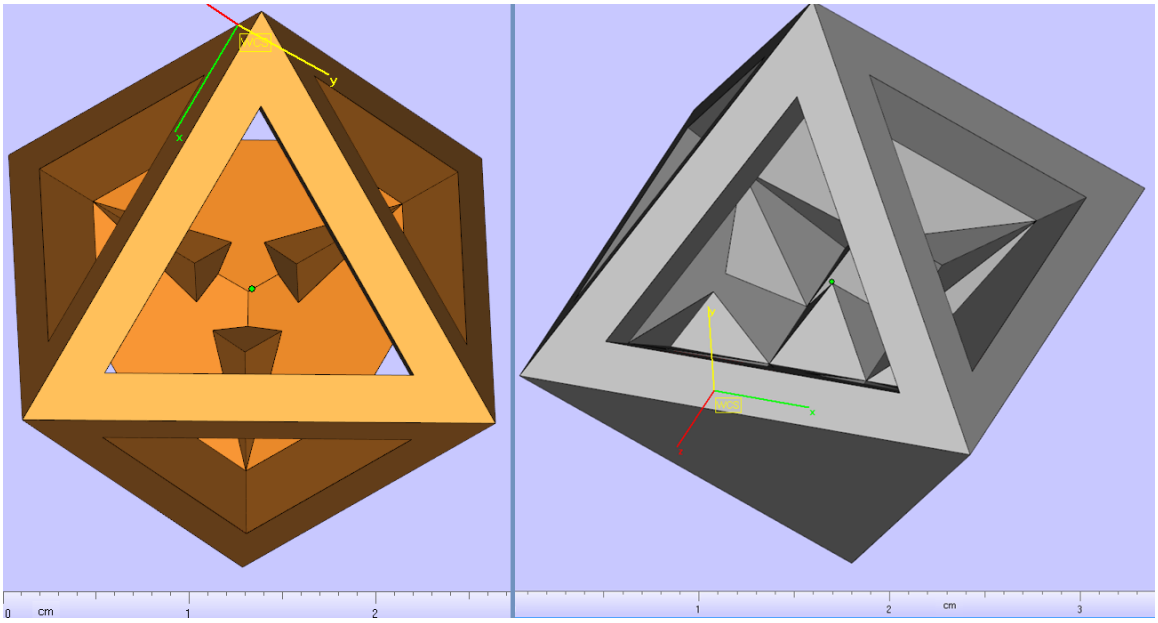

Figure 61. CAD image of the 7/8-cut octahedron (left) and the 1/2-cut octahedron (right).

5.7.1 Print Details

As with the cube, both octahedrons were oriented to stand on the build plate by its respective corners with the uncut solid triangular surfaces facing downward. In this orientation, none of the component faces were less than 45° to the build plate. However, in an attempt to reduce peeling and thermal warpage, a unique combination of ‘Contour’, ‘Line’, and ‘Web’ support structure types were generated to increase the anchoring contact between the components and the build plate (Figure 62).

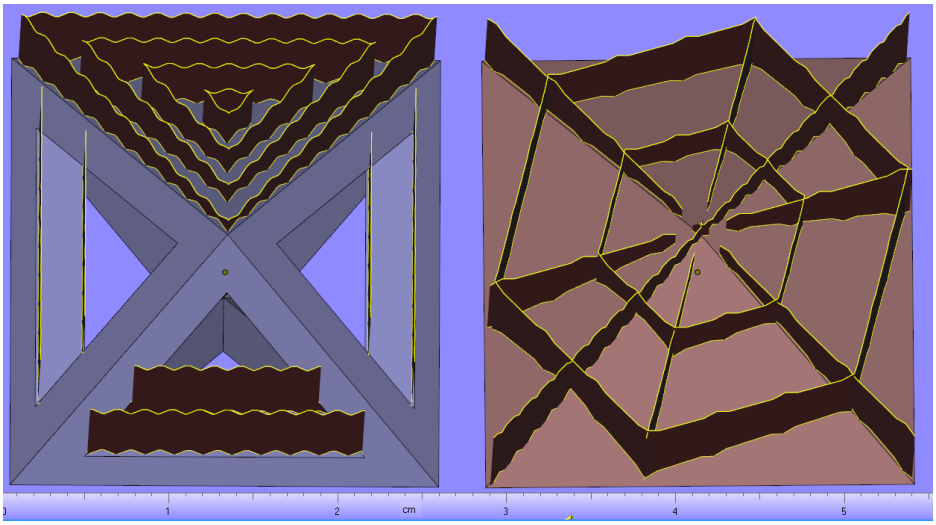

Figure 62. CAD image of the contour and web support structures attached to the 7/8-cut octahedron and 1/2-cut octahedron, respectively.

Both octahedrons exhibited significant burn-in, melt percolation, and unsatisfactory dimensional tolerance attributable to recoater damage from component peel-off and the subsequent misalignment of previously solidified layers (Figure 63, Figure 64). As with the cube, these may be traced back to insufficient anchoring of the fixed-free cantilever beams.

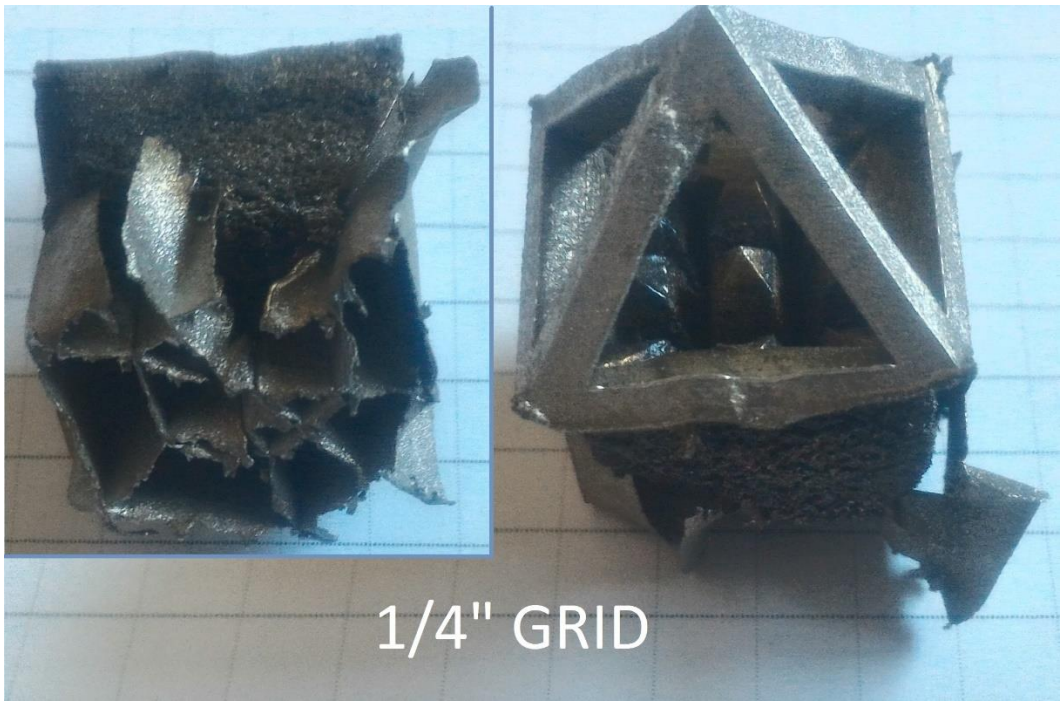

Figure 63. As-printed 1/2-cut octahedron. Significant melt percolation protrudes from the downward facing surfaces.

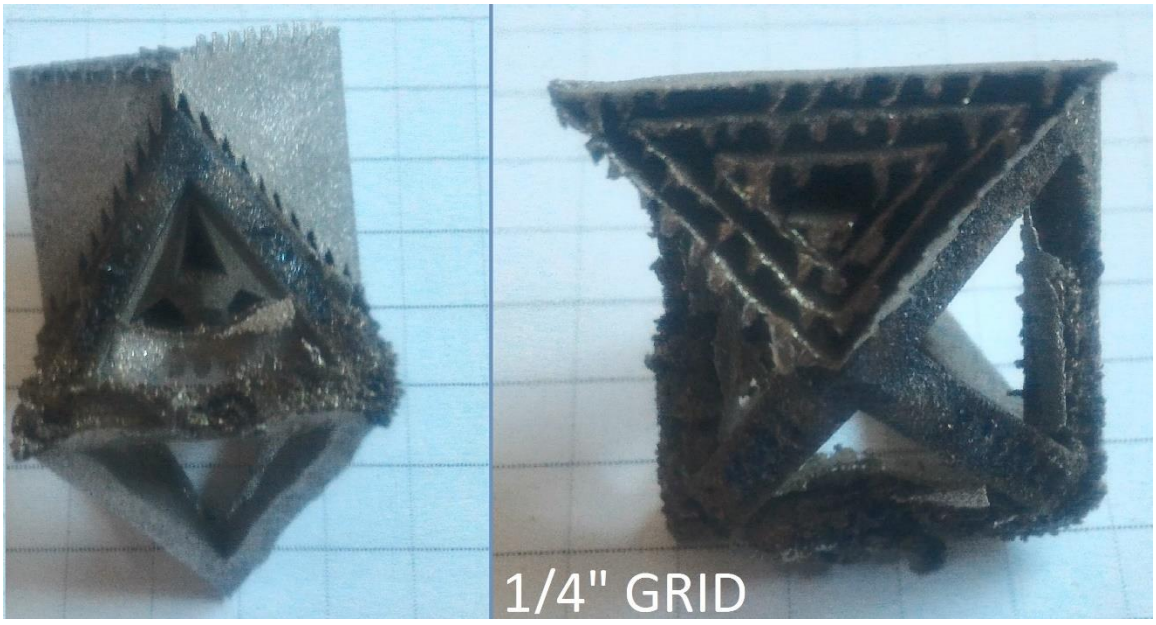

Figure 64. As-printed 7/8-cut octahedron. Burn-in and mild melt percolation covers the downward facing surfaces of the octahedron members.

5.8 BCC Lattice Compression Specimen

A 20 mm x 20 mm x 20 mm cuboidal lattice consisting of 512 (2.5 mm x 2.5 mm x 2.5 mm) unit cells was modelled in SolidWorks to evaluate different lattice geometries in compression loading (Figure 65). Each unit cell consists of four 0.5 mm thick vertical (90°) circular struts at each corner with eight 45° 0.5 mm thick circular struts meeting at the middle, resembling a crude BCC cell. Horizontal (0°) struts are not present in the unit cell. As a secondary objective, the component also evaluated the print resolution of the machine, the effect of residual stresses for symmetrically patterned 45° thin members, and the spatial support structure requirements for 0° overhanging surfaces.

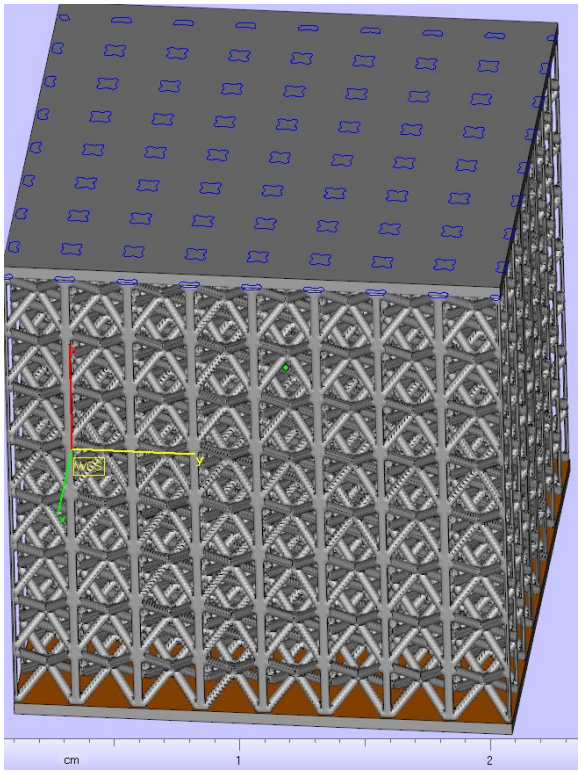

Figure 65. CAD image of the BCC Lattice Compression Specimen. Lattice-to-top-plate connections outlined in blue.

5.8.1 Print Details

The component was oriented with its lower plate parallel (0°) to the build platform (Figure 66). In this orientation, the component had one overhanging surface: the underside of the top-plate. This surface was supported by 0.5 mm thick circular columns spaced 2.5 mm in a grid pattern. The bottom surface was supported by the default 'Block' support structure type.

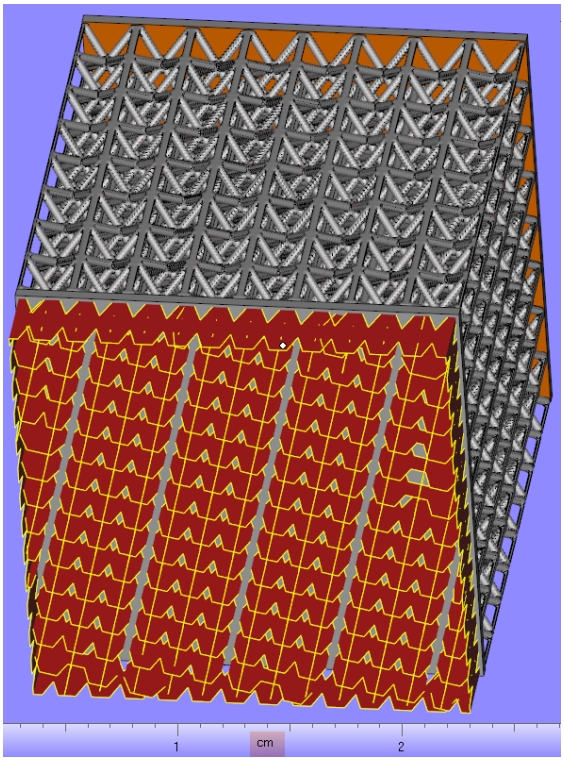

Figure 66. CAD image of the block-type support structures on the bottom-plate of the BCC Lattice Compression Specimen.

In general, the lattice printed successfully with excellent dimensional tolerance and regularity. The 45° cross-struts show no evidence of melt percolation and the surface finish of the component is consistent.

Upon close inspection, the underside of the top plate shows significant melt percolation manifesting as a bowed, 5.0 mm-deep U-shaped slump with its lowest point

at the center of the component. The topside of the top plate is slightly concave, with most of the sloped deformation occurring around the outer edges of the component. The topside middle of the top plate is absent of evidence indicative of the melt percolation occurring on the reverse side.

5.8.2 Lessons Learned

The lattice geometry interfacing with the underside of the top plate provided inadequate support. To contrast, the default block-type support structure geometry consisting of 1.0 mm-wide cross (+) columns spaced in a 1.5 mm grid pattern shows satisfactory results. Future lattice geometries that interface with an overhanging surface should maintain as many points of contact as possible with minimal spacing.

5.9 IME Radial Card Holder Memento

A 4cm diameter card holder consisting of 12 fins attached to a 2.5 mm thick baseplate was modelled in SolidWorks to hand-out to guests at the LLNL-Cal Poly partnership ceremony on June 2nd, 2017 (Figure 67). 2.5 mm tall letters spelling out "CALPOLY IME" were debossed into 10 of the 12 fins. The purpose of the component is to hold business cards vertically in the 1.75 mm gaps between each fin.

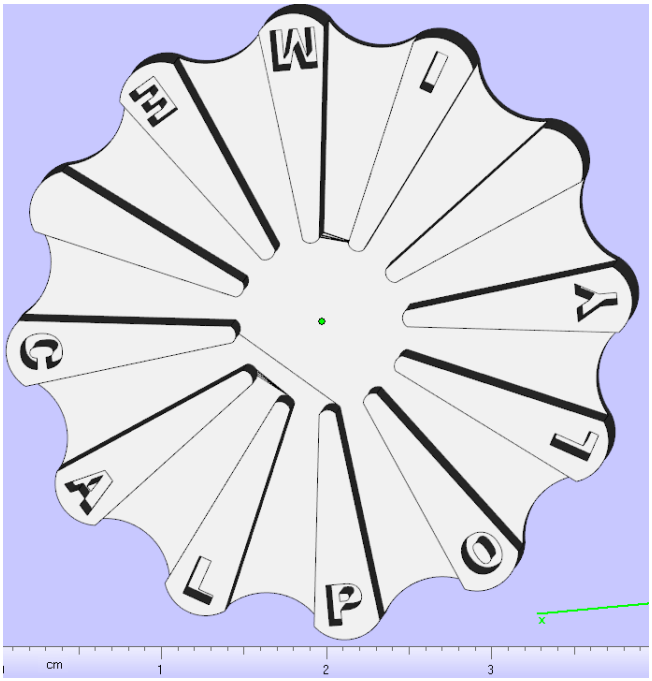

Figure 67. CAD image of the IME Radial Card Holder Memento.

5.9.1 Print Details

The baseplate bottom surface was aligned parallel to the build plate and supported with the default ‘Block’ support type. Two copies of the component were printed with three other parts in two consecutive prints for a total of four radial card holder mementos (Figure 68). In both prints, the left-side of the print bed in the vicinity of the “IME” lettering had poor powder coverage, resulting in the incomplete formation of the component. Conversely, the right-side component exhibited adequate powder coverage and fabricated successfully in both prints (Figure 69). The cause of this discrepancy will be investigated by SLM technicians in a follow-up visit.

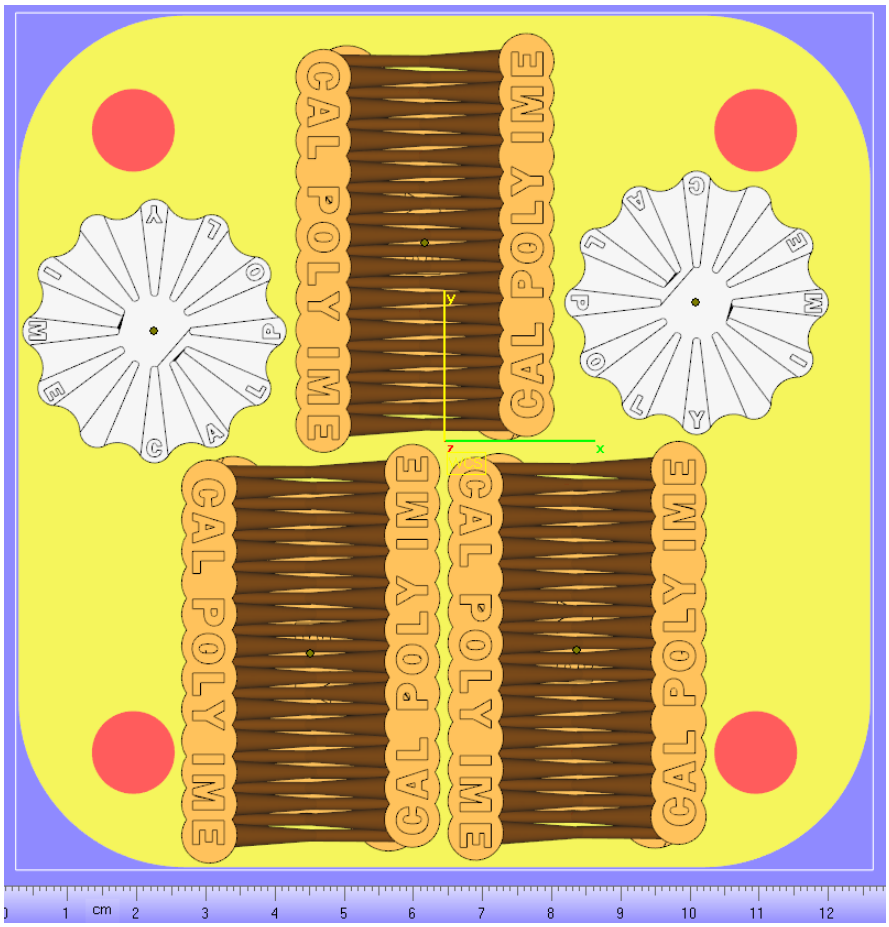

Figure 68. Top-down view of the Magics build plate with 2 IME Radial Card Holder Mementos and 3 IME Strut Card Holder Mementos.

Figure 69. Top-down view of an IME Radial Card Holder Memento printed on the right-side of the build plate.

5.10 IME Strut Card Holder Memento

A 60 mm x 38 mm x 57 mm card holder consisting of 24 interlocking struts lofted from a 2.5 mm baseplate was modelled in SolidWorks as a secondary hand-out to guests at the LLNL-Cal Poly partnership ceremony on June 2nd, 2017 (Figure 70). The letters CAL POLY IME" and "LEARN BY DOING" were debossed into the upper strut platforms and baseplate, respectively. The struts are variable in diameter, starting at 2.0 mm at the baseplate to the interlocking mid-length, increasing to 4.0 mm at the base of the platform, and increasing again to 8.0 mm at the maxima of the platform.

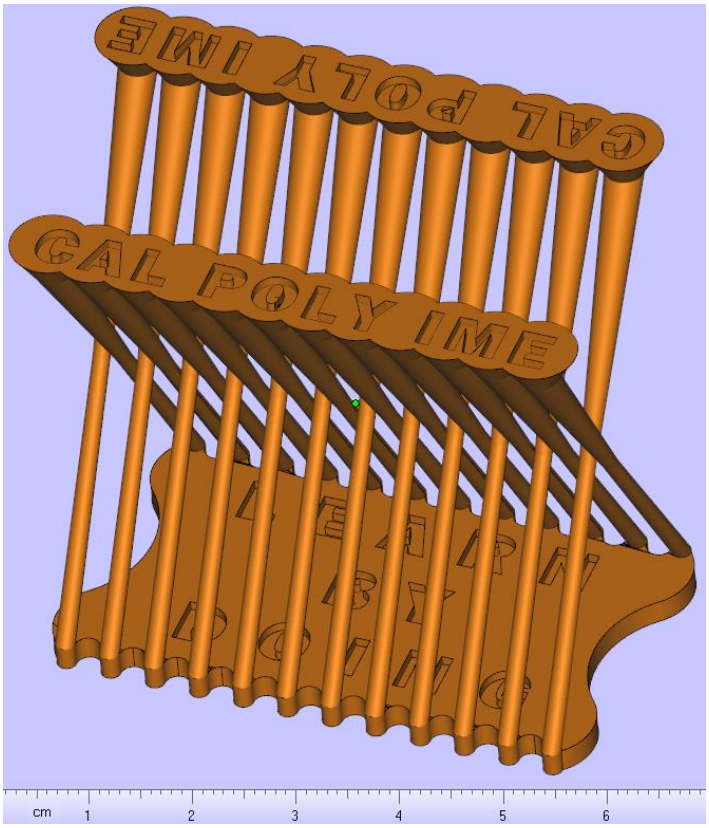

Figure 70. CAD image of IME Strut Card Holder Memento.

5.10.1 Print Details

The baseplate was oriented parallel to the build plate and supported with the default “Block” support structure type. The component was printed successfully without any design-related complications arising during fabrication.

The debossed letters and strut diameters show excellent dimensional resolution that accurately represents the original design (Figure 71). The outer struts relative to the platform show a slight inward warpage, likely caused by thermal contraction occurring at the first couple layers of continuous platform generation. Despite this apparent residual stress, the struts can be flexed considerably without damaging the component.

Figure 71. As-printed IME Strut Card Holder Memento.

6 Laying the Foundation for Future Research

The 7th California Polytechnic State University learning objective for students is to "engage in lifelong learning". One may interpret this as the current student's responsibility to facilitate the learning of those that follow him or her, thereby promoting the education of others for posterity. As part of this interpretation, a significant objective of this thesis is to lay the foundation for future research and learning with the SLM 125 HL. This was achieved through the extensive generation of standard operating procedures (SOP), templates, checklists, and general guidelines related to the machine and its operation. It is the hopes of the author to instill a sense of duty in all potential SLM operators to contribute and improve upon the education and research opportunities of future generations of students.

6.1 Standard Operating Procedures

Due to the inherent safety risks of the process and the potential to cause significant damage, the SLM 125 HL shall only be operated by students of at least junior standing. For this reason, the average lifetime of an operator is expected to be around 2 years. As the operation of the SLM 125 HL is no trivial manner, an extensive time investment for training is required for each student. To facilitate this process, detailed SOPs have been generated for use on Cal Poly's campus through the Dozuki platform (calpolyime.dozuki.com).

Dozuki's centralized management, customizable templates, historical data management, and clean features provide an excellent framework for live documentation of the SLM process. Numerous benefits, such as a reduction in time investment for

training new operators and the standardization of practices to reduce the introduction of operator variability, are provided by maintaining high quality SOPs.

The following SOPs are planned, in-progress, or completed at the time of writing:

- Starting a Build
- Resuming a Build
- Ending a Build
- Using Magics to generate .SLM Files
- Sieving Powder with the PSM 100
- Replacing the Recoater Blade
- Replacing the Recoater Top-Plate
- Resurfacing a Used Build Plate
- Cleaning the Build Chamber and its Peripherals
- Replacing the Primary Filter

6.2 Templates, Checklists, and Guidelines

In addition to SOPs, a variety of templates, checklist, and general guidelines have been prepared to assist with the documentation efforts. The philosophy behind each document is to provide a means of concise and effective knowledge transfer to past, present, and future operators. The following documents are planned, in-progress, or completed at the time of writing:

- Preliminary Build Summary Template
- Failure Analysis Report Summary Template (Examples in Appendix)
- Preliminary Build Logsheet Template
- Design for SLM Guidelines

BIBLIOGRAPHY

Abele, E., Stoffregen, H. A., Kniepkamp, M., & Lang, S. (2015). Selective laser melting for manufacturing of thin-waleld porous elements. *Journal of Materials Processing Technology*, 114 - 122.

Aydogdu, G. H., & Aydinol, M. K. (2006). Determination of susceptibility to intergranular corrosion and electrochemical reactivation behavior of AISI 316L type stainless steel. *Corrosion Science*, 3565 - 3583.

Bertoli, U. S., Wolfer, A. J., Matthews, M. J., Delplanque, J.-P. R., & Schoenung, J. M. (2016). On the Limitations of Volumetric Energy Density as a Design Parameter for Selective Laser Melting. *Materials & Design*.

Cooper, K., Steele, P., Cheng, B., & Chou, K. (2016). *Contact-free support structures for part overhangs in powder-bed metal additive manufacturing.* Huntsville, AL: Marshall Space Flight Center.

Hussein, A., Hao, L., Yan, C., & Everson, R. (2013). Finite element simulation of the temperature and stress fields in single layers built without-support in selective laser melting. *Materials and Design*, 638 - 647.

Institute, A. I. (1988). *Welding of Stainless Steels and Other Joining Methods.* Metals Park, OH: Nickel Development Institute.

Khairallah, S. A., Anderson, A. T., Rubenchik, A., & King, W. E. (2016). Laser powder-bed fusion additive manufacturing: physics of complex melt flow and formation mechanisms of pores, spatter, and denudation zones. *Acta Materialia*, 36 - 45.

King, W. E., Barth, H. D., Castillo, V. M., Gallegos, G. F., Gibbs, J. W., Hahn, D. E., . . . Rubenchik, A. M. (2014). Observation of keyhole-mode laser melting in laser

powder-bed fusion additive manufacturing. *Journal of Materials Processing Technology*, 2915 - 2925.

Liu, Y., Yang, Y., Mai, S., Wang, D., & Song, C. (2015). Investigation into spatter behavior during selective laser melting of AISI 316L stainless steel powder. *Materials & Design*, 797 - 806.

Materialise. (2015). *SLM Build Processor User Guide.* Leuven, Belgium: Materialise.

Matthews, M. J., Guss, G., Khairallah, S. A., Rubenchik, A. M., Depond, P. J., & King, W. E. (2016). Denudation of metal powder layers in laser powder bed fusion processes. *Acta Materialia*, 33 - 42.

Mertens, R., Clijsters, S., Kempen, K., & Kruth, J.-P. (2014). *Optimization of Scan Strategies in Selective Laser Melting of Aluminum Parts with Downfacing Areas.* Journal of Manufacturing Science and Engineering.

Montero Sistiaga, M. L., Nardone, S., Hautfenne, C., & Van Humbeeck, J. (2016). Effect of heat treatment of 316L stainless steel produced by selective laser melting (SLM). *Solid Freeform Fabrication Symposium*, (pp. 558 - 565). Austin, Texas.

Murray, J., Cooper, A. R., & Nagy, J. (1964). *Explosibiltiy of Metal Powders.* Washington D.C.: United States Department of the Interior Bureau of Mines.

Otsu, D., Muetterties, N., & Lovejoy, T. (2016). *Metals Additive Manufacturing Powder Aging Characterization.* San Luis Obispo, CA: California Polytechnic State University.

Patterson, A., Messimer, S., & Farrington, P. (2017). Overhanging Features and the SLM/DMLS Residual Stresses Problem: Review and Future Research need. *Technologies*.

Saeidi, K. (2016). *Stainless steels fabricated by laser melting.* Department of Materials and Environmental Chemistry. Stockholm, Sweden: Stockholm University.

SLM Solutions Group. (2014, April 7). *Company Presentation.* Retrieved from MostTech: https://www.mosttech.at/content/userfiles/files/SLM%20Solutions_Company%20presentation_07.04.2014.pdf

SLM Solutions Group AG. (2017, June 23). *SELECTIVE LASER MELTING MACHINE SLM 125*. Retrieved from SLM Solutions: https://slm-solutions.com/products/machines/selective-laser-melting-machine-slm-125

Strano, G., Hao, L., Everson, R. M., & Evans, K. E. (2013). Surface roughness analysis, modelling and prediction in selective laser melting. *Journal of Materials Processing Technology*, 589-597.

Vora, P., Mumtaz, K., Todd, I., & Hopkinson, N. (2015). *AlSi12 in-situ alloy formation and residual stress reduction using anchorless selective laser melting.* Additive Manufacturing.

Washko, S., & Aggen, G. (1990). Wrought Stainless Steels. In *Properties and Selection: Irons, Steels, and High-Performance Alloys* (pp. 841-907). ASM International.

Yusuf, S. M., Chen, Y., Boardman, R., Yang, S., & Gao, N. (2017). *Investigation on porosity and microhardness of 316L stainless steel fabricated by selective laser melting.* Basel, Switzerland: Metals.

Zhong, Y., Liu, L., Wikman, S., Cui, D., & Shen, Z. (2016). Intergranular cellular segregation network structure strengthening 316L stainless steel prepared by selective laser melting. *Journal of Nuclear Materials*, 170- 178.

APPENDIX

Failure Analysis Report – Build 0005

Compiled by: David Otsu Last updated: June 22, 2017

Estimates, speculation, or missing information are colored accordingly.

Build Details

See build summary for more information.

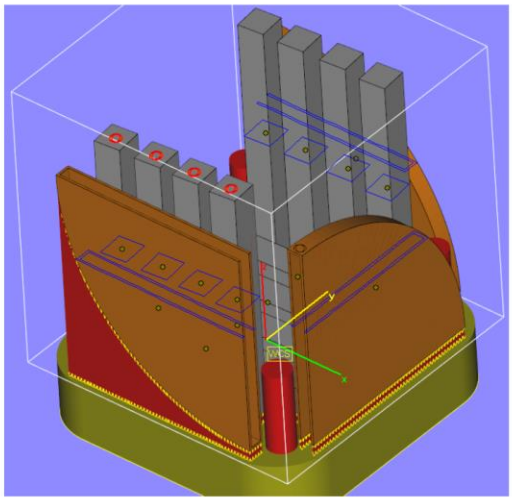

Figure 1. CAD view of Build 0005. Layer at failure outlined in blue.

Summary of Events

Build 0005 was initialized on 04/21/2017 (Friday) at 1307 hours. On 04/22/2017 at 1859 hours, the LCS detected an error in the powder bed and interrupted the build. The interrupted build was discovered by operator David Otsu on 04/24/2017 (Monday) at 1349 hours. Since the build had been interrupted for a significant amount of time at a layer containing dimensionally critical components, the decision was made to completely halt the build.

Visual inspection of the build chamber revealed the following information:

- There was inadequate powder coverage on the right-side of the build volume (Figure 2)
- The left-side powder gate cam screw had fallen off and come to rest at the rear of the build chamber (Figure 3)
- The right-side recoater clamp had come loose and lowered significantly, first signified by excessive rattling during recoater movement and verified by hand once the recoater was removed from the chamber (Figure 4)
- The top-plate of the recoater had lowered significantly, resulting in an increase in the powder-gate to recoater gap (Figure 5)

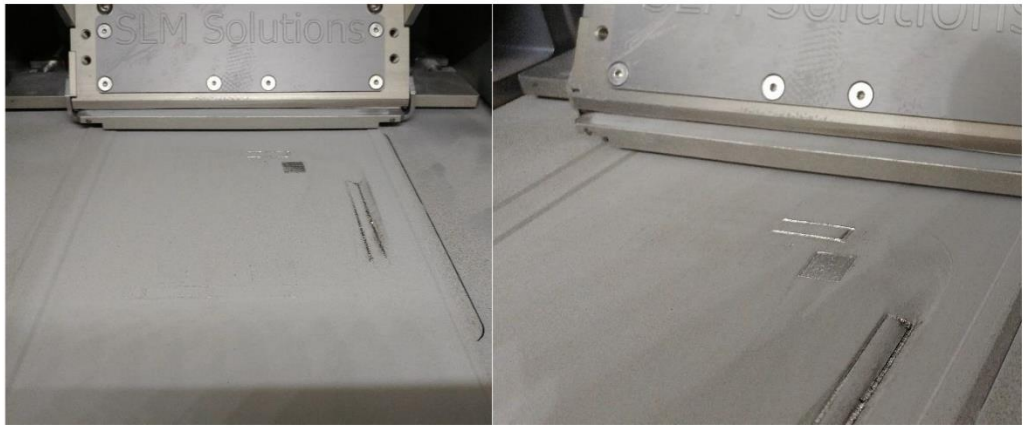

Figure 2. Poor powder coverage on the righr side of the plate, affecting the right-side FullScale_QuarterCircle_NoLattice, the far-right rear Tensile Oversized V3, and the right-side of the rear FullScale_QuarterCircle_NoLattice.

Figure 3. Left-side powder gate cam screw resting at the rear of the build chamber as discovered after removing the recoater.

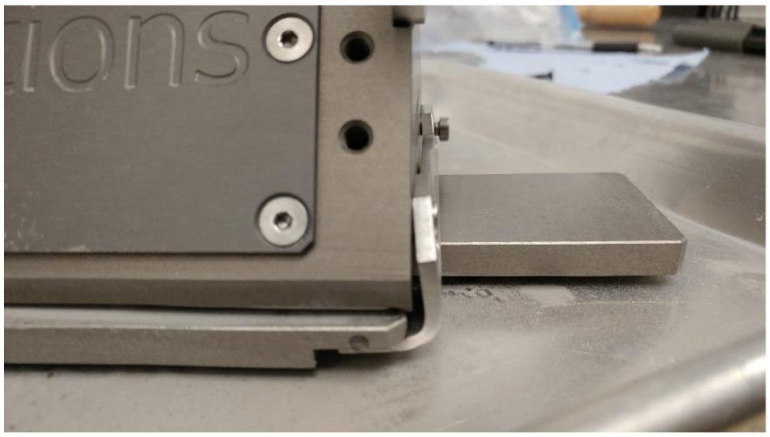

Figure 4. The right-side recoater clamp in an insecure state.

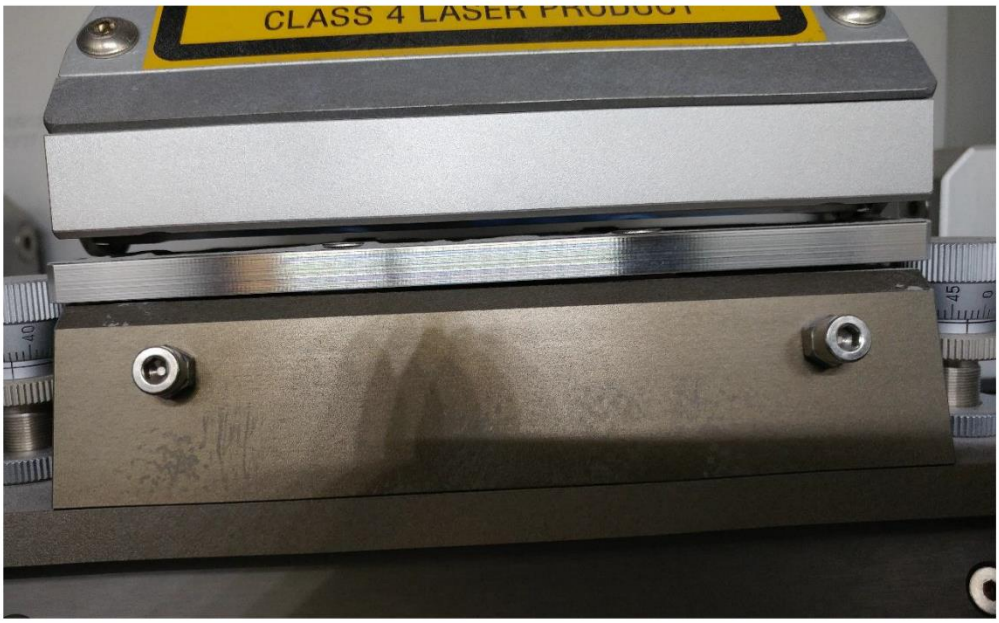

Figure 5. The large powder-gate to recoater gap resulting from the lowering of the top-plate.

The left-side powder gate cam screw was reinstalled successfully. Correspondence with SLM Solutions established tightening the cam screws before every build as the corrective action. The right side recoater clamp was re-adjusted and secured successfully.

Additional Sensor and Software Evidence

N/A

Additional Physical Evidence

FullScale_QuarterCircle_NoLattice (Stripe Parameter Set) Deformation and Failure

The right-side FullScale_QuarterCircle_NoLattice was fabricated using the stripe parameter set. Visual inspection of the component revealed significant support structure delamination and bulging along the quarter-circle thin wall. The chess parameter set FullScale_QuarterCircle_NoLattice exhibited no such deformation. It is believed that the high-aspect ratio thin-walls accumulated thermal stress across the build, eventually resulting in complete yield and fracture along the support structure interface, the weakest section of the build assembly. This component failure is not expected to have contributed significantly to the overall build failure, as there is no evidence of recoater blade damage or powder blockage resulting from the delamination.

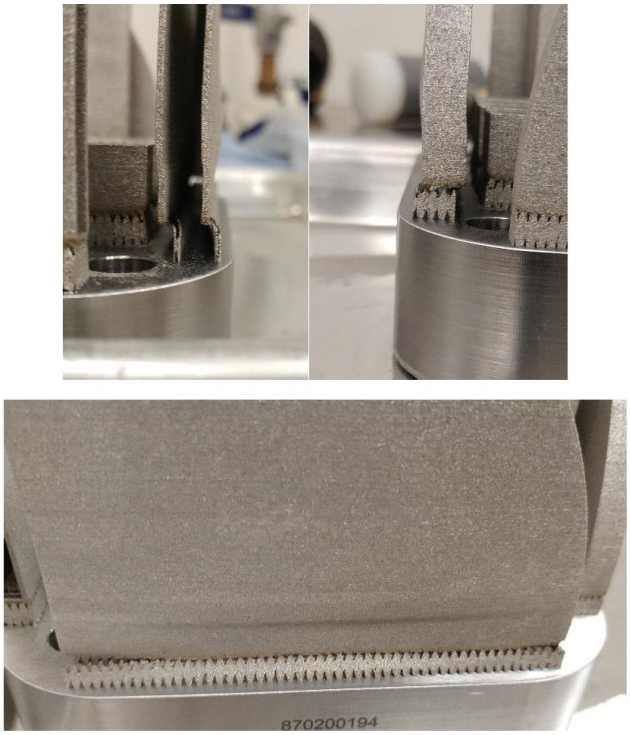

Figure 6. Delamination of the FullScale_QuarterCircle_NoLattice component fabricated with the default stripe parameter set.

Proposed Mode of Failure

The build was interrupted by the LCS due unsatisfactory powder layer coverage. The unsatisfactory powder layer coverage occurred on the right side of the build plate.

Proposed Mechanism of Failure

The unsatisfactory powder coverage is believed to have resulted from an unacceptable increase in powde-gate to recoater distance, potentially compounded by the left-side powder gate cam screw hardware malfunction. If the gap is too large between the powder-gate and the recoater, the cams will fail to fully actuate and dispense an entire layer's worth of powder. This can manifest on just the left or right hand side, depending on which cam fails to actuate completely. The insufficient powder dispensing occurs gradually over the ~30 layers prior to the build interrupt. There is no evidence of recoater damage or component-induced powder blockage on the build plate contributing to the LCS interruption.

Path Forward

The powder-gate cams shall be tightened prior to every build. The friction between the cams and the recoater top-plate shall be monitored. Should the friction increase to the point where the powder chute lurches when the recoater moves forward, the diamond sanding block shall be used to smoothen the cam and top-plate surfaces until the unsatisfactory friction is suppressed.

The stripe parameter set is not appropriate for components with high aspect ratio cross-sections. The residual stresses generated from this scan pattern may overcome the yield strength of the component-support structure interface, resulting in significant deformation and the potential for overall build interruption.

OPERATOR OPINION: Additionally, it is recommended to turn off the LCS when the build cannot be monitored for its entire duration (as is the case with overnight or weekend long builds) and the fabricated components have relatively small XY footprints. Although this may waste consumables, there is the possibility that the malfunction only affects a sub-section of the entire build plate. This gives the unaffected components a chance to successfully fabricate at the cost of the malfunctioning sub-section.

Estimates, speculation, or missing information are colored accordingly.

Build Details

See build summary for more information.

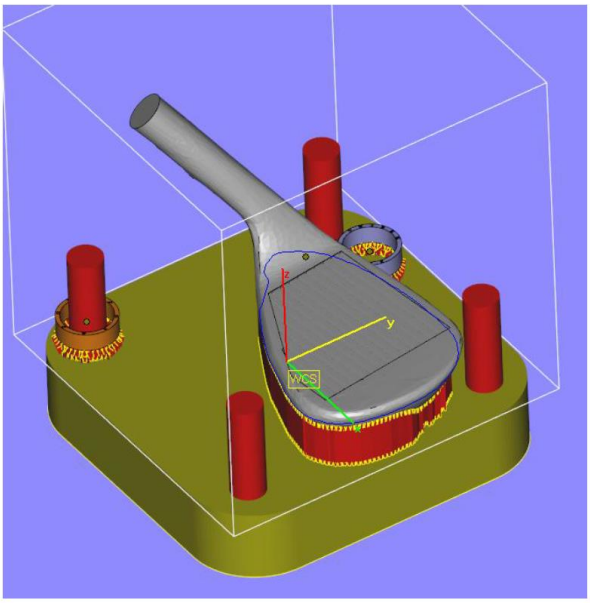

Figure 1. CAD view of Build 0009. Failure layer outlined in blue.

Summary of Events

The build was initialized at 1500 hours on 05/05/2017. At 1850 hours on 05/05/2017, the Cabinet 2 temperature exceeded its upper limit of 45°C. As per standard procedure, the MCS interrupted the build on the 445th layer to wait for further instructions from a human operator. The high outdoor temperature for the day was 88°F.

The following day, operator David Otsu analyzed the interrupted build chamber surface and observed no signs of in-situ defects or malfunctioning hardware. As the part being printed (NWYControlWedgeFinal) was not flagged as dimensionally critical at the layer of interruption, the build was resumed at 1300 hours on 05/06/2017. The Cabinet 2 temperature again exceeded its upper limit, tripping a build interrupt at 1422 hours on 05/06/2017 on the 600th layer. The high for the day was 87°F.

Operator David Otsu made the decision to halt the build completely, as the outdoor temperature was not expected to decrease significantly until the end of the week.

Additional Sensor and Software Evidence

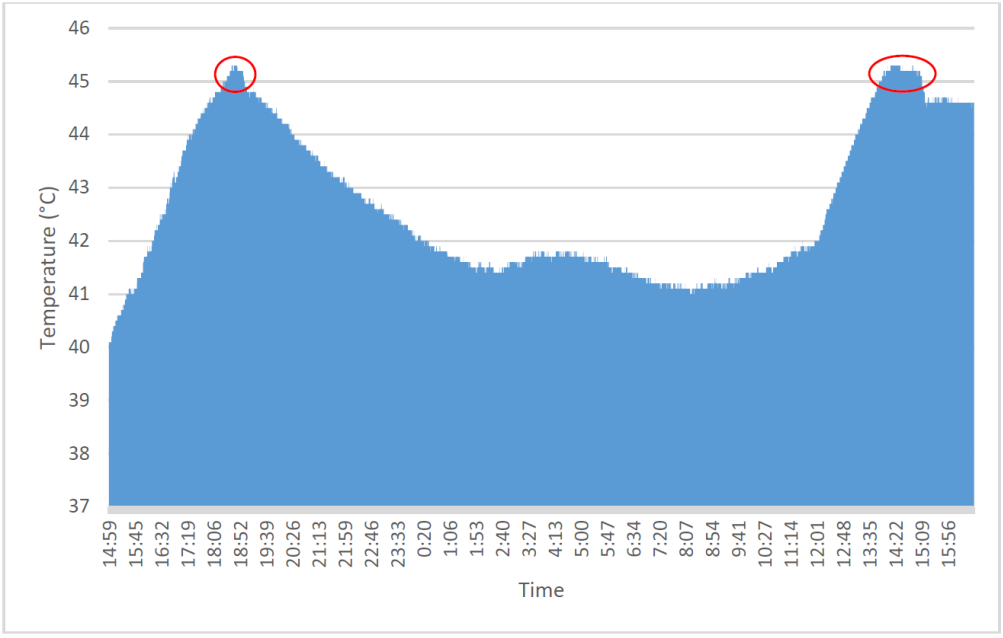

Figure 2. Temperature log of Build 0009. Unacceptable temperature peaks labelled in red.

Additional Physical Evidence

Build Plate and Print Quality

The unfinished NWYControlWedgeFinal shows a distinct change in surface quality at the layer of interruption. The post-interruption surface is darker and rougher than the pre-interruption surface.

Support structures in the process of being generated at the layer of interruption exhibit a significant discontinuity. Discontinuity line is parallel to the layer of interruption, as opposed to following the weaker connecting joints along the surface of the golf club.

Additionally, the unfinished NWYControlWedgeFinal component shows significant melt layer percolation along the wide edge of the club. The outer surface near the percolation is degraded significantly.

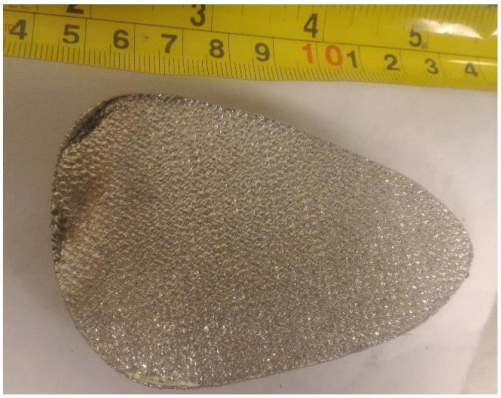

Proposed Mode of Failure

Both interrupts were the result of Cabinet 2 exceeding its upper limit of 45°C. There is no evidence of SLM hardware or software malfunction contributing to the interruptions.

Proposed Mechanism of Failure

Overall Print

The build chamber exceeded its upper limit because the room in which the SLM is installed was at too high of an ambient temperature.

Effects on NWYControlWedgeFinal

The interruption drastically affected the in-process NWYControlWedgeFinal. Surface quality degradation, discontinuities, and percolation defects are apparent in the post-interruption sections of the component. Oxygen logs show no evidence of atmospheric degradation. The presence of significant defects may be attributed to shifts in position of the underlying parts as a result of the prolonged resting time and sudden changes in heating/cooling rates upon restart. The characteristic 'burn-in' coloration has been seen in other components that shift significantly mid-build (from peel-off, thermal warpage, etc.)

Path Forward

The acceptable ambient temperature for successful SLM operation appears to peak around 85°F. The AC unit from IME computer lab was repurposed for the SLM room on 05/05/2017. Ambient temperature is no longer expected to exceed 76°F. The build shall be re-attempted during the week of 05/08/2017.

New Instructions

The condensation tank shall be monitored daily until a drainage line can be installed. The AC unit airflow shall not be directed at the SLM build chamber or the operating table under any circumstances. The AC unit intake filter shall be inspected monthly for cleanliness.

Failure Analysis Report – Build 0012

Compiled by: David Otsu Last updated: June 7th, 2017

Estimates, speculation, or missing information are colored accordingly.

Build Details

See build summary for more information.

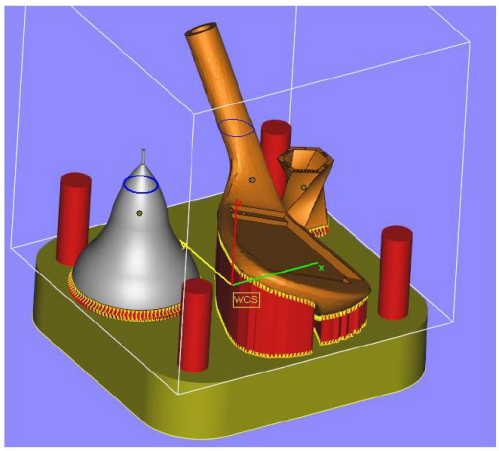

Figure 1. CAD image of Build 0012. Layer of interruption outlined in blue.

Summary of Events

Build 0012 was loaded and initialized on the evening of May 09th, 2017. At layer 1500, the MCS received a positioning error from the recoater system and interrupted the build.

Subsequent visual inspection revealed that the front-right underside powder chute door screw had come loose, protruding 1/8 inch down from the lip of the powder chute (). The screw prevented the recoater from returning to its refill position under the powder chute. The screw head shows significant deformation resulting from the recoater running into it. Scratches on the recoater top-plate implies that the screw came loose across multiple layer cycles until it protruded enough to obstruct the recoater completely.

Figure 2. Stick-out of the front-right side powder gate screw that resulted in the obstruction of recoater motion.

The damaged screw was removed successfully. Attempts to completely install a fresh screw were unsuccessful, indicative of internal thread damage within the powder chute. The damaged hole shows a 1/16 inch difference in maximum insert depth when compared to the undamaged holes. An on-site visit by the West Coast SLM Solutions technician Manual Amborsius confirmed the thread damage inside the powder chute. The thread was re-tapped and a fresh screw was installed successfully. However, significant cracking along the chamber wall facing side of the powder chute as found. The location of the cracks suggest they are the result of the recoater pulling the powder chute away from the wall when the cams seize against the top plate. A replacement powder chute and powder gate were ordered.

Figure 3. Cracks in the powder chute along the chamber wall facing side.

Additional Sensor and Software Evidence

N/A

Additional Physical Evidence

Build Plate and Print Quality

2in_doublebell_half_thickness_outerSLDPRT and NWYControlWedgeFinal were not completed due to the interruption. None of the three parts in the build show abnormal print quality.

Proposed Mode of Failure

The build was interrupted by a MCS positioning error of the recoater system.

Proposed Mechanism of Failure

The positioning error was caused by the loosening and resulting obstruction of recoater movement by the front-right underside powder chute screw.

Path Forward

Continue to run builds with the damaged powder chute, minimizing build height when possible. Install the new powder chute and powder gate once **both** components are available. Install screws with low strength Loctite to avoid a similar problem in the future. Closely monitor the recoater top plate and powder gate cams for seizing.

Failure Analysis Report – Build 0015

Compiled by: David Otsu Last updated: June 8, 2017

Estimates, speculation, or missing information are colored accordingly.

Build Details

Build 0015 consisted of one "h_15" part, designed and optimized by LLNL to purposely fail at a specific layer (Figure 1). The build plate heating element was shut off and the LCS was de-activated to facilitate the failure. The corresponding senior project group personally monitored the build for the majority of its duration.

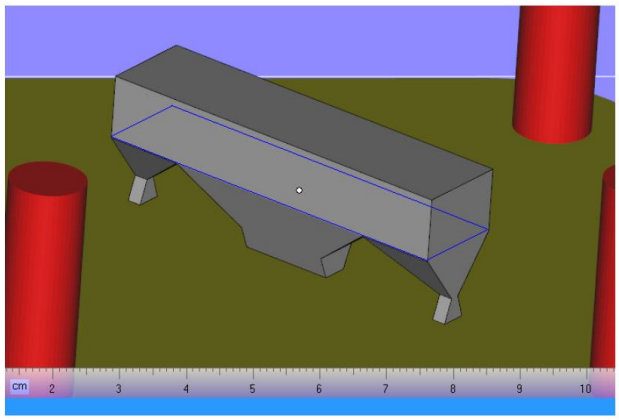

Figure 1. Isometric view of h_15. Expected failure layer is outlined in blue.

Summary of Events

Build 0015 was initialized on 05/23/17 at 1049 hours and completed on 05/23/17 at 1407 hours. The monitoring senior project group noticed the gradual development of powder track marks around the expected layer of failure indicative of recoater blade damage. Inspection of the post-build chamber revealed deep powder tracks corresponding to the same positions initially reported by the senior project group. Subsequent examination of the recoater blade revealed wear and tear that spatially correlates with the powder tracks.

Figure 2. Power bed tracks and the corresponding damaged recoater blade.

The component itself shows significant warpage and upward peeling of its two outer legs, corresponding well with the failure mode predictions proposed by LLNL. As with the powder tracks, the outer legs spatially correlate with the recoater blade wear and tear. The component sub-sections above the expected failure layer show dimensional instability resulting from the uneven powder caused by the damage sustained to the recoater blade.

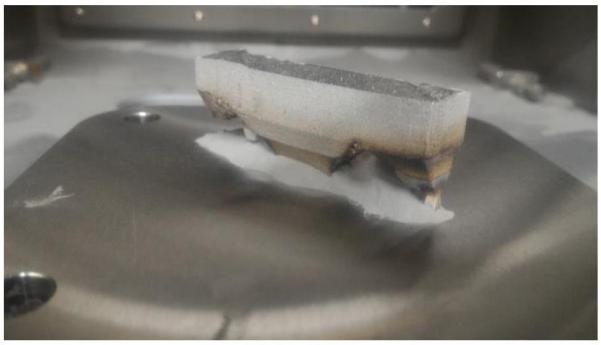

Figure 3. As-printed h_15 component with failed outer legs and burn-in characteristic of poor dimensional stability.

Additional Sensor and Software Evidence

N/A

Additional Physical Evidence

N/A

Proposed Mode of Failure

N/A

Proposed Mechanism of Failure

N/A

Path Forward

Should a component failure result in damage to the recoater blade, other components that share the recoater path will also be detrimentally affected. Thus, components that are likely to fail should not share the recoater path with other independent components (Figure 4).

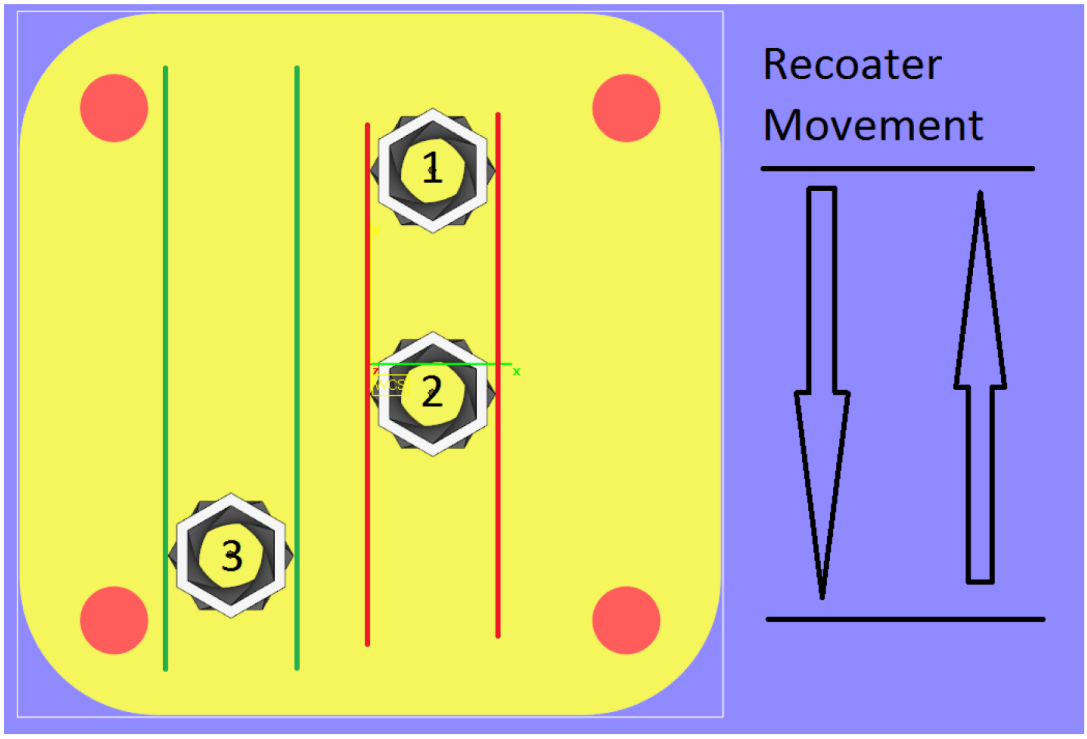

Figure 4. Example of proposed recoater stay-out zone. Component 1 and 2 share the same recoater path (red) and are therefore improperly placed. Conversely, Part 3 does is not sharing a recoater path (green) with any other component and is therefore properly placed.

Estimates, speculation, or missing information are colored accordingly.

Build Details

See build summary for more information.

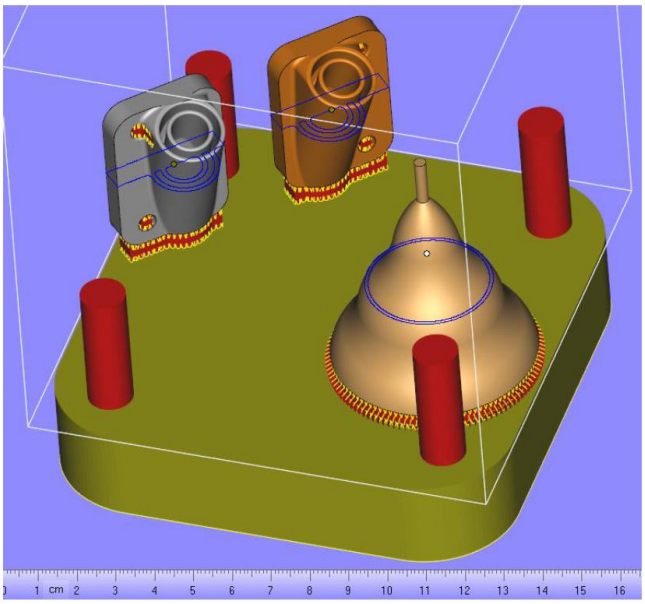

Figure 1. CAD image of Build 0015. Layer at failure outlined in blue.

Summary of Events

Build 0016 was initialized on 05/24/2017 at 1326 hours. At 1814 hours, around the 900th layer, the pressure differential across the main chamber filter reached an unacceptable limit and forced an interruption of the build. The dirty filter and the primary filter container was removed and a new filter in the backup filter container was installed.

During installation of the new filter, operator David Otsu attempted to vacuum the remnant particles on the chamber-side channel. This resulted in a blow-back of particles into the build chamber, covering the powder bed and recoater in large chunks of soot and necessitating extra clean-up (Figure 2). No evidence of irreversible damage or extraordinary contamination was found after clean-up.

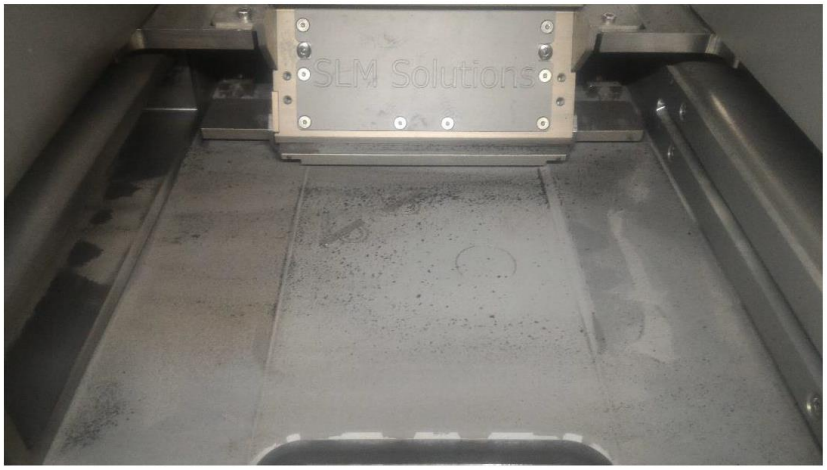

Figure 2. Blowback of soot after vacuum attempt.

Review of the initial training period revealed that the SLM trainer recommended replacing the filter whenever the max pressure differential line approached the red zone. The SLM trainer related anecdotes of filter replacements occurring anywhere between every other build (1-2 days) to every week (5 days). The max pressure differential line was not monitored closely up to this build.

Additional Sensor and Software Evidence

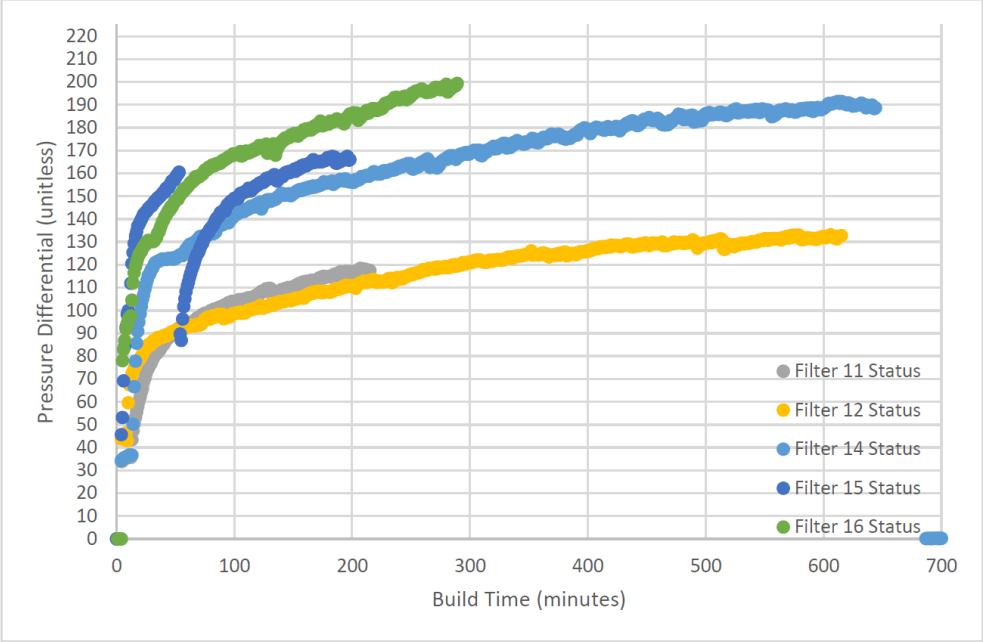

Figure 3. Filter status readouts from previous builds. MCS auto-interrupts the build when the pressure differential exceeds 200 units Build-to-build trend fairly consistent. Reason for discontinuity of Build 0015 unknown.

Additional Physical Evidence

N/A

Proposed Mode of Failure

The build was interrupted by the MCS due to an pressure differential across the main chamber filter.

Proposed Mechanism of Failure

Through normal usage, the main chamber filter became over-saturated with soot particles, necessitating its replacement. There are no indications of abnormal filter or sensor behavior.

Path Forward

The max pressure differential of every build shall be monitored closely. Should the linear depiction approach the red zone, the filter shall be replaced.